SPAWAR
Systems Center
PACIFIC

TECHNICAL REPORT 3056
February 2017

Quasi-static Design of Electrically Small Ultra-Wideband Antennas

Thomas O. Jones III

SSC Pacific
San Diego, CA 92152-5001

SSC Pacific
San Diego, California 92152-5001

G. M. Bonitz, CAPT, USN
Commanding Officer

C. A. Keeney
Executive Director

ADMINISTRATIVE INFORMATION

The work described in this report was performed by the Electromagnetics Technology Branch (Code 52260) of the Systems of Systems (SoS) and Platform Design Division (Code 52200), Space and Naval Warfare Systems Center Pacific (SSC Pacific), San Diego, CA.

Released by
M. Osburn, Head
Electromagnetics Technology Branch

Under authority of
J. McGee, Head
Systems of Systems (SoS) and
Platform Design Division

The citation of trade names and names of names of manufacturers is not to be construed as official government endorsement or approval of commercial products or services referenced in this report.

SB

EXECUTIVE SUMMARY

Ultra wideband antennas (UWB) can be designed with electrostatic methods using a generalization of the [1] asymptotic conical dipole (ACD). The electrostatic methods allow the antenna Q-factor to be calculated for a large number of antenna designs without numerically solving Maxwell's Equations. The ACD uses a constant line charge distribution and image line charge distribution (both on the z-axis) to generate equipotential surfaces. Each equipotential surface represents an ACD antenna design with a different height. In the *Q*uasi-static Antenna Design Algorithm [2, 3, 4, 5, 6] the antenna designs fit within a 1-meter sphere. Both the charge distribution and charge distribution geometry are varied to generate a range of antenna shapes. The Q-factor ratio, radiation resistance, and capacitance design curves are calculated from the geometry and charge distribution. Each charge distribution and geometry represents a unique antenna shape and surface charge density. Solutions are selected from the design curves, then the antenna shape is calculated; the last step is numerical electromagnetic modeling of the antenna. For the UWB antenna designs, the charge distribution is on a cone and an image cone. The charge distribution on the cone and the image cone is selected to give a conical feed point. The cone half angle and cone length are the geometric parameters used to generate the Q-factor ratio, radiation resistance, and capacitance design curves. The minimum Q-factor, radiation resistance, and capacitance for the UWB antenna designs are plotted as a function of the charge distribution half cone angle. In this plot, the radiation resistance and capacitance are discontinuous. This discontinuity is caused by the absolute and local ratio minimum in the Q-factor ratio design curve. The discontinuity occurs when two different charge distribution cone geometries give the same Q-factor ratio. Three antennas, 50-, 30-, and (the minimum Q-factor ratio) 32-Ω input impedance designs that are numerically modeled from 30 MHz to 2.5 GHz. The antenna impedance and voltage standing wave ratio (VSWR) is calculated. In all models, the VSWR drops sharply to about 1.2:1, then drops to 1.1:1 for nearly all of the frequency range. The Smith chart, time domain feed point input, and feed point reflection are plotted. The minimum Q-factor ratio design has a 3:1 VSWR at 42.67 MHz or an antenna height of one-seventh of a wavelength at the lowest operational frequency and 8.34 wavelengths at the highest operational frequency.

CONTENTS

Figures

Tables

1. INTRODUCTION

The ultra wideband (UWB) antenna shape determines both the lowest operating frequency and Q-factor ratio. For electrically small antennas, the quasi-static antenna design algorithm can be used to design very low Q-factor ratio antennas with high bandwidth [4, 5]. The Q-factor ratio is the coefficient of the largest term in Chu's limit, the right side of Equation (1) [7]. Lowering the Q-factor ratio reduces the Q-factor for the electrically small part of the frequency range. The UWB antenna shape in the quasi-static antenna design algorithm is a cone with an attached bulb. The lowest operational frequency is reduced without increasing the voltage standing wave ratio (VSWR) at higher frequencies. This is a physics-based algorithmic approach that avoids the typical cut-and-try method.

In 1948, Chu [7] established a lower bound for the Q-factor (inverse bandwidth) of an antenna. Chu's limit is calculated from the energy stored in the electromagnetic field. The antenna is enclosed within a sphere with a radius a; only the stored energy outside the sphere is included in the limit. The energy inside the sphere is zero. For top-loaded monopoles, the energy is electrostatic below the antenna's resonant frequency and magnetic above the antenna's resonant frequency. At resonance, the electric and magnetic energy are equal but 90° out of phase. The top-loaded monopoles have a large reactance and stored magnetic energy above resonance. On the other hand, the UWB antennas have small reactance and stored magnetic energy above resonance. In UWB antennas, the Q-factor is ~ 1 above the lowest operational frequency.

An infinite bi-conical (transmission line) is a UWB antenna with a constant impedance; the cone angle determines the impedance. A finite bi-conical antenna was patented by Oliver Lodge [8, 9]. In his design, the end of the cone reflects the outgoing wave back into the feed point. Thus, the antenna is no longer UWB or constant impedance. Reducing this reflection from the top of the cone is a longstanding problem. The Schelkunoff and Friis [10] teardrop antenna (bi-cone at feed point) improves the performance. Kraus's volcano and smoke antenna design was an effort to eliminate the reflection from the antenna. Paulson, West, Perger, and Kraus [11] state that the volcano and smoke monopole is typically one-fourth a wavelength high. Maloney and Smith [12] used resistive material in the cone to absorb the reflection from the top of the cone; this reduces the antenna efficiency. The Ice Cream Cone (ICC) monopole designed by Simpson, Pavlovic, and Olcan [13] does not use resistive material. The combined spherical bulb and cone has no reflection from the feed point. The ICC antenna height is one-fifth of the longest operational wavelength[1]. For a 1-meter monopole, the lowest operational frequency is 60 MHz. Another approach to the UWB antenna design is the exponential taper of Hale Simonds [14] and hyperbolic cosine taper of Thomas O. Jones III [15]; this design reduces the width of the antenna, which implies that the bulb shape can be non-spherical at high frequencies.

The stored energy in an UWB antenna is analyzed differently. The cone is a transmission line that supports an outgoing, freely propagating wave; the outgoing wave does not represent stored energy. The transmission line is terminated with a bulb. The bulb reflects some of the radio-frequency (RF) energy back into the transmission line to the feed point. This reflected energy, an incoming wave, is included in the stored energy and in the Q-factor. The bulb also contributes directly to the stored energy. The bulb shape is the critical factor in determining the Q-factor. For a fixed cone angle, the cone plays no role in the Q-factor. This report presents a scientific method for designing low Q-factor UWB bulb shapes.

[1] Personal communication with Ted Simpson.

The Quasi-static Antenna Design Algorithm is used to design a minimum Q-factor bulb shape with a conical feed point. The algorithm uses electrostatic methods [2, 3, 4, 5, 6]. In electrically small antennas, the magnetic fields are small and can be neglected, which permits the use of the quasi-static approximation used in the algorithm. A static charge distribution is used to generate equipotential surfaces. The equipotential surfaces are perfect conductors with $E_{\|} = 0$. Each equipotential surface represents a unique antenna surface and surface charge density. For an antenna, the charge is only on the surface of the conductor. The Quasi-static Antenna Design Algorithm requires the charge distribution to be enclosed by the equipotential surfaces.

The antenna Q-factor is calculated from radiation resistance, R_{Rad}, the capacitance C, the angular frequency $\omega = 2\pi f$:

$$Q = \frac{1}{\omega C R_{Rad}} = \frac{Q_{Factor\ ratio}}{(ka)^3}, \tag{1}$$

where f is the frequency. The Q-factor ratio ($Q_{Factor\ ratio}$) is calculated from Q and ka, where $k = 2\pi/\lambda$, where λ is the wavelength, and a is the enclosing spheres radius. The radiation resistance is calculated from the effective height and the effective height is calculated from charge distribution. The capacitance is calculated from the peak scalar potentials on the enclosing sphere [2, 3]. For a fixed DC voltage V, higher capacitance increases the stored energy $E = CV^2/2$. For a fixed charge Q, increasing the capacitance decreases the stored energy $E = Q^2/2C$. The Quasi-static Antenna Design Algorithm used a fixed charge on the monopole arm. The Quasi-static Antenna Design Algorithm was used to compute the thick-disk-cap monopole [13, 14]. The charge disk height and radius describe the geometry of the thick-disk charge distribution. The charge distribution on the disk uses five multipoles. The thick-disk-cap monopole required only seven unknowns [4, 5, 6] to converge to the solution. Above the thick-disk-cap monopole resonance, this design has a 37% lower Q-factor than the spherical-cap monopole design (the best known top-loaded monopole design). The approximations in the Quasi-static Antenna Design Algorithm is discussed by Thomas O. Jones III in [5, 6].

The Quasi-static Antenna Design Algorithm requires a charge distribution that generates a wide range of cone and bulb shapes. The z-axis line charge distribution used in [2, 3] does not model the general bulb shape. A rotationally symmetric three-dimensional conical charge distribution models the bulb shape and the conical feed point. Figure 1 is a MATLAB® plot of the 50-Ω input impedance UWB antenna with a 120° cutaway showing the conical charge distribution. The color is the magnitude of the surface charge density/m^2 on the antenna and cone. The surface charge density/m^2 is smaller on the antenna than the cone. The charge on the antenna is spread over a larger surface area; this significantly reduces the surface charge density. In addition, the image cone reduces the electric field and surface charge density above the bulb. The image cone increases the electric field and surface charge density near the feed point of the antenna.

Section 2 calculates the effective height for the conical charge distribution. The charge distribution is selected to give a very good approximation of a 50-Ω cone. This conical charge distribution reduces to a line charge on the z-axis (cone half angle $\psi = 0$). The normalized radiation resistance, $R_{Rad}/(ka)^2$ is computed as a function of charge-distribution-cone half angle and fractional cone length (*length /a*). Section 3 develops a numerical method to calculate the scalar potential for the general conical charge distribution. The numerical method uses $2N$ wires to model the charge distribution [14, pp. 43–56 for the cylinder]. The error in this numerical model is a very small, high-order multipole moment in the scalar potential. The high-order multipole moment error decreases with

increasing *N*. The capacitance is computed as a function of charge-distribution-cone half angle and fractional cone length.

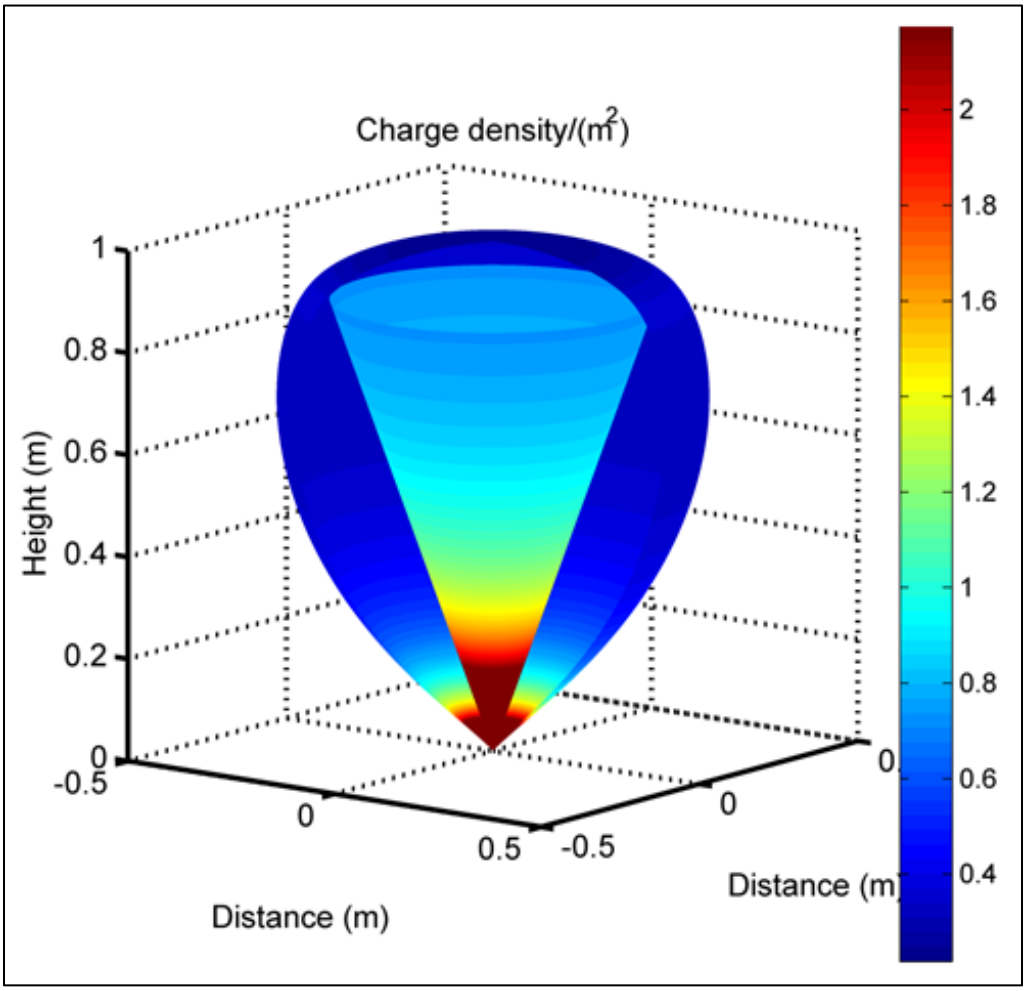

Figure 1. The 50-Ω input impedance antenna shape (equal-potential surface) with a 120° slice removed to show the conical charge distribution. The color is the charge/m^2. The antenna surface charge is spread over a much larger surface area, thus it is lower than the surface charge on the cone.

Section 4 calculates the Q-factor ratio as a function of the charge-distribution-cone half angle and fractional cone length. The Q-factor ratio design curve is discussed in great detail in Section 4. For low-charge distribution-cone half angles, the radiation resistance has a moderate value. At a critical charge distribution-cone half angle, the radiation resistance jumps to a much higher value. At higher charge distribution-cone half angles, the radiation resistance drops, the capacitance increases, and the Q-factor ratio drops to a minimum of 3.265. The antenna parameters are calculated for several antenna input impedances: 50 Ω, 30 Ω, and for the minimum Q-factor antenna, 32 Ω. The feed point is a very good approximation of the 50-Ω input impedance cone. The 50- and 30-Ω designs touch the enclosing sphere at the top. The minimum Q-factor antenna, 32 Ω, touches the enclosing sphere on the side. The minimum Q-factor antenna, 32-Ω input impedance, designed with this simple model, does not fill the top of the sphere. A more complex model would fill the top of the sphere and reduce the antenna Q-factor.

In Section 5, computer simulation technology (CST) is used to compute the impedance of the 50- and 30-Ω input impedance antennas and the minimum Q-factor antenna, 32 Ω, where the VSWR is 3:1 at 43.1, 40.1, and 39.3 MHz, respectively. The VSWR drops very quickly to a VSWR of $\sim$ 1.2:1; then the VSWR is $\sim$1.1:1 up to 2.5 GHz. In Section 6 is the conclusion. The Quasi-static Antenna Design Algorithm generates three UWB non-spherical bulb shapes. The non-spherical bulb shape performs as well as the spherical bulb. A more complex conical charge distribution would provide a lower Q-factor design by extending the length of the cone and increasing the size of the bulb. Minimizing the Q-factor ratio may increase the VSWR at higher frequencies, which could be caused by an edge on the antenna surface. A different antenna design near the minimum Q-factor ratio could give a smoother antenna surface, which would reduce the reflection from the edge without significantly increasing the Q-factor ratio of the antenna.

2. CONICAL CHARGE DISTRIBUTION AND EFFECTIVE HEIGHT FOR UWB ANTENNA

The effective height was computed [2, 3] for an asymptotic conical dipole (ACD) and a linear charge distribution (LCD) [3]; both charge distributions are on the z-axis of the dipole. A linear combination of these two charge distributions can create a conical feed point for a UWB antenna; however, the bulb shape is nearly spherical and similar to the ICC antenna.

A rotationally symmetric conical shaped charge distribution can model both the feed point and bulb shape of the UWB antennas. The surface charge $\sigma(\imath)$ is integrated around a ring at position $\imath$. The total charge on this ring is defined as a simple linear function on l

$$q(l) = (1-\alpha)\frac{1}{ka} + \alpha\left(\frac{2l}{(\kappa a)^2}\right) = \int_0^{2\pi} \rho(l)\sigma(l)d\theta, \tag{2}$$

where κa is the cone length, a is the radius of the enclosing sphere, $\imath$ is the distance to the ring, and ρ is the radius of the ring. The fractional cone length is dimensionless, $0 < \kappa < 1$. The parameter $\alpha = 0.35$ gives a very good approximation of a 50-Ω input impedance cone at the feed point. The charge-distribution-cone half angle ψ (measured from the z-axis) and κ, the fractional cone length, generate a family of UWB antenna designs. For the charge-distribution-cone half angle $\psi = 0$, Equation (2) reduces to a linear combination of the ACD and LCD with the charge distribution on the z-axis.

The effective height depends only on the height of the charge on the z-axis. The radius and height of the ring of charge is $\rho = \imath \sin\psi$ and $z = l\cos\psi$, respectively.

$$q(-l)_{image} = -q(l)_{monopole}, \tag{3}$$

the charge as a function of z, is

$$q(z) = q(z/\cos\psi)/\cos\psi\,, \tag{4}$$

which is plotted in Figure 2.

The surface charge density on the antenna (with a 120° slice removed) and cone is plotted in Figure 1. The antenna and cone have the same net charge; however, the charge on the antenna is spread out over a larger surface area, which significantly reduces the surface charge density on the antenna. The image cone also reduces the electric field and surface charge density on the bulb's top. The image cone increases the electric field and surface charge density near the feed point. The surface charge on the cone is

$$\sigma_s(l) = q(l)/(2\pi\rho(l)) \qquad . \tag{5}$$

Note: $\rho \to 0$ and as $\sigma \to \infty$. The net charge on the ring is finite. For display purposes, the range of values plotted is limited to $\sigma_s \le 10 * \min(\sigma_s)$. The charge distribution on the monopole arm is normalized to give

$$q_{Total} = \int_0^{\kappa a} q(l)\,dl = 1. \tag{6}$$

The effective height is easily calculated as

$$h_{Eff} = \frac{1}{q_{Total}} \int_0^{\kappa a} q(l) z \, dl = \frac{1}{q_{Total}} \int_0^{\kappa a \cos \psi} \frac{q(z/\cos \psi)}{\cos \psi} z \, dz. \tag{7}$$

This reduces to

$$h_{Eff}(\kappa, \psi) = \left[(1-\alpha) \frac{\kappa a}{2} + \alpha \frac{2\kappa a}{3} \right] \cos \psi. \tag{8}$$

The radiation resistance is calculated from the standard equation

$$R_{Rad}(\kappa, \psi) = 40 k^2 h_{Eff}^2, \tag{9}$$

where $k = 2\pi/\lambda$ and λ is the wavelength. Figure 3 is a plot of $R_{Rad}(\kappa, \psi) / (ka)^2$ as a function of the cone geometry ψ and κ. $R_{Rad}(\kappa, \psi)/(ka)^2$ is independent of frequency and the enclosing sphere's radius a.

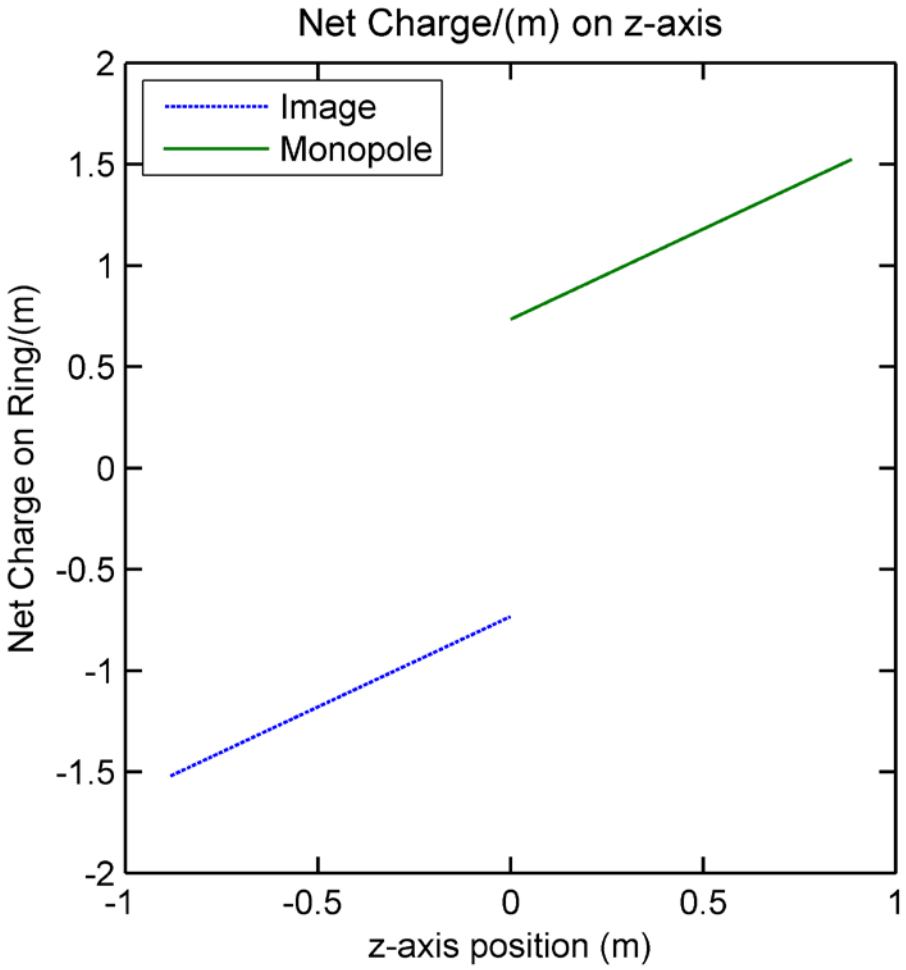

Figure 2. The 50-Ω input impedance monopole and image charge distribution on a ring is integrated to give q_z net charge/m at each point on the z-axis. The feed point is at z = 0.

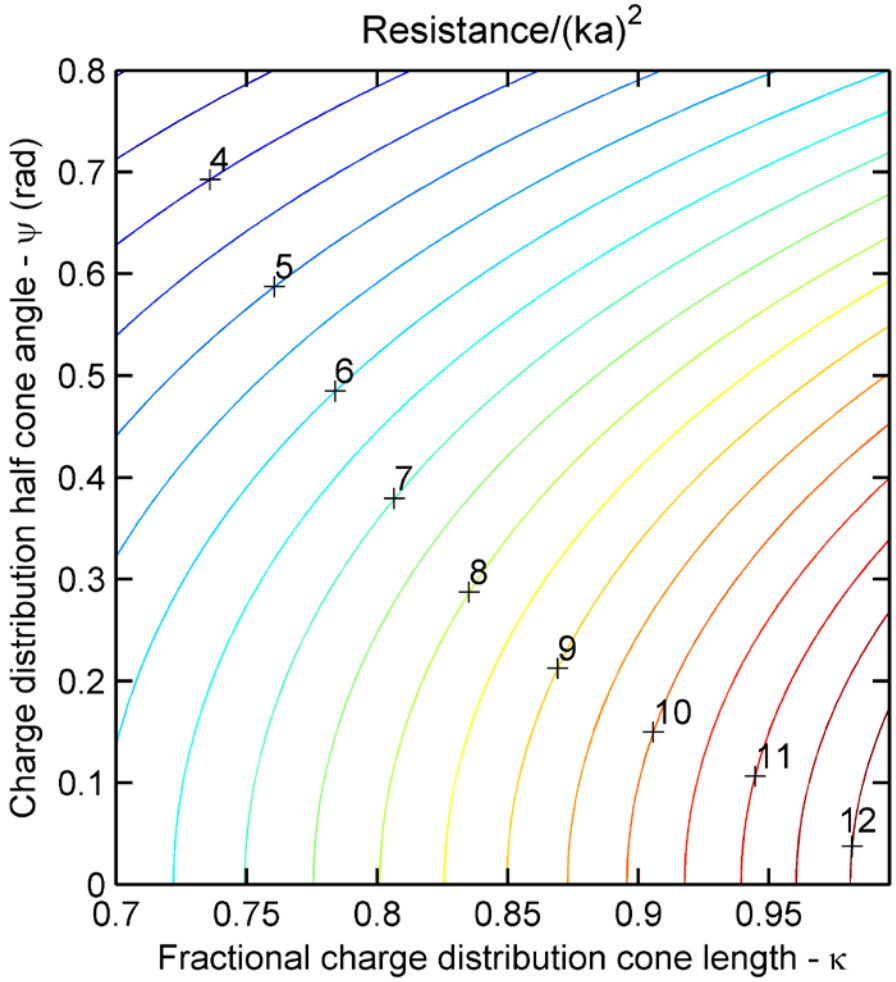

Figure 3. $R_{Rad}\,(\kappa, \psi)/(ka)^2$ as a function of the charge distribution geometry κ and ψ, which is computed from the effective height of the charge distribution.

3. CAPACITANCE FOR UWB ANTENNA DESIGN

The capacitance is computed from the net charge on the dipole arm and the maximum scalar potential on the enclosing sphere. The scalar potential for the cone charge distribution is rotationally symmetric *(z, ρ)* where ρ is the radial distance from the z-axis and z is the position on the z-axis. The rotational symmetry reduces the scalar potential calculation to the x-z plane.

The cone-charge-distribution scalar potential is computed by replacing the cone's surface with 2*N* wires running from the charge distribution bi-cone's bottom edge to the charge distribution bi-cone's top edge. Figure 4 shows how wires are used to approximate the conical charge distribution, *N = 2* and *N = 6*. The blue solid and dash lines represent the *N = 2* wire approximation. The blue solid and dash lines are symmetric about the x-z plane. The *N = 6* wire approximation uses the *N = 2* results. The red dash-dot and dot lines represent the eight additional wires required for the *N = 6* wire approximation. The red dash-dot and dot lines are also symmetric about the x-z plane. Only half of the wires (solid and dash-dot) are needed in the numerical method. The cylindrical version of this numerical approximation is discussed in detail in [16]; the sequence of wire approximations *N*, 3*N*, 9*N*,...,$3^m N$ etc. reuses all of the previous calculations, which was suggested by Lance Koyoma.

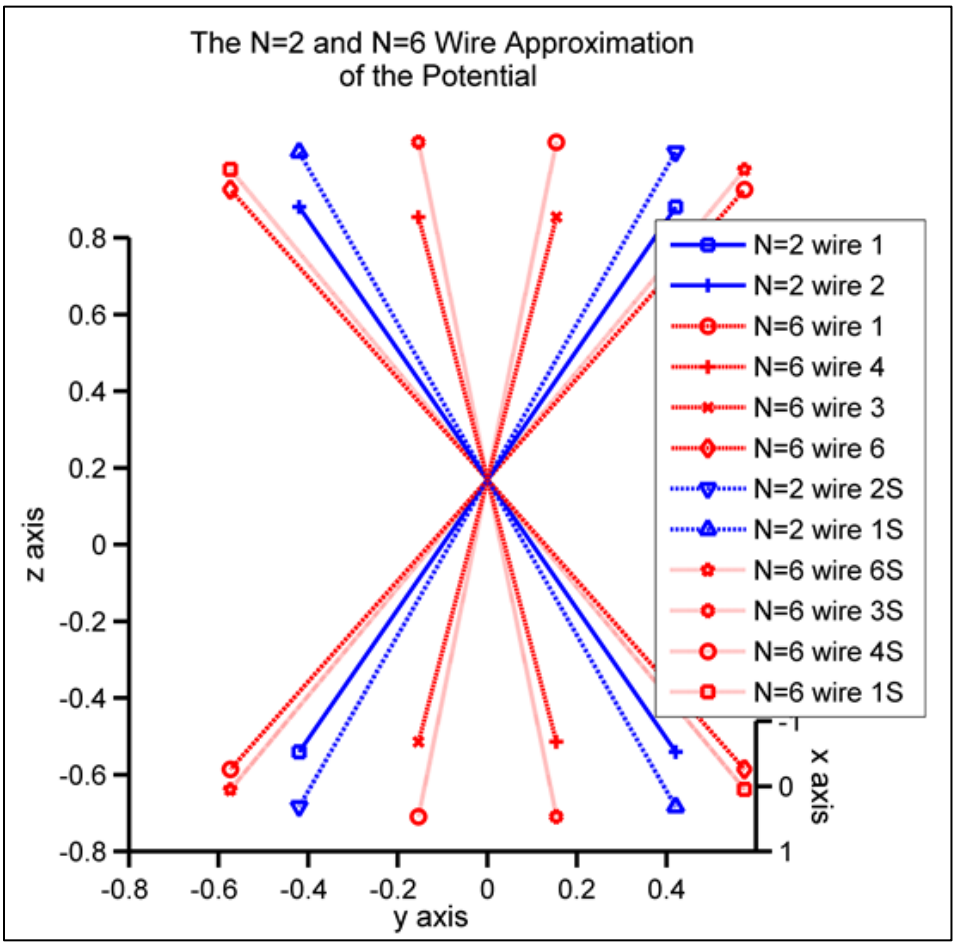

Figure 4. The 2-wire (blue) and 6-wire (red) numerical approximation of the cone charge distribution.

The scalar potential for the ACD was previously computed [2, 3] (a constant line and image charge on the z-axis). The following equation includes the image monopole:

$$\Phi^{ACD}(z,\rho) = \frac{1}{4\pi\varepsilon_0 \kappa a} \ln\left[\frac{(1+\delta_m)(1-\delta_i)}{(1-\delta_m)(1+\delta_i)}\right], \tag{10}$$

where $\delta_m = \kappa a/(R_f + R_t)$ is for the monopole and $\delta_i = \kappa a/(R_f + R_b)$ is for the image monopole with a unit net charge on each arm. In this case, the quantities R_t, R_f, and R_b are the distance from the field point (z, ρ) to the top of the wire, feed point, and the bottom of the wire, respectively. The scalar potential for the linear charge distribution (LCD) on the z-axis, $2P_1(z'/\kappa a)/(\kappa a)$, was previously calculated [3]:

$$\Phi^{LCD}(z,\rho) = \int_{-\kappa a}^{\kappa a} \frac{2P_1(z'/\kappa a)}{\kappa a\sqrt{(z'-z)^2+\rho^2}} dz' = \frac{2z}{(\kappa a)^2}\left[\ln\left(\frac{1+\tau}{1-\tau}\right) - 2\tau\right], \tag{11}$$

where $\tau = 2\kappa a/(R_t + R_b)$ and z' is z-axis integration variable for the charge distribution and the net charge on the arm is

$$1 = \frac{2}{\kappa a}\int_0^{\kappa a} P_1(z'/\kappa a)\, dz'. \tag{12}$$

The next step is to compute R_t, R_f, and R_b for the wire on the cone. The wire is rotated φ radians around the x-axis; $\varphi = 0$ on the x-z plane. The cone half angle is ψ radians from the z-axis. The wire end point at the top cone edge is

$$z_t = a\kappa\cos\psi \tag{13}$$
$$y_t = a\kappa\sin\psi\sin\varphi \tag{14}$$
$$x_t = a\kappa\sin\psi\cos\varphi. \tag{15}$$

The same wire end point on the bottom cone edge is

$$z_b = -a\kappa\cos\psi \tag{16}$$
$$y_b = -a\kappa\sin\psi\sin\varphi \tag{17}$$
$$x_b = -a\kappa\sin\psi\cos\varphi. \tag{18}$$

The distance from the top cone edge to the point (z, ρ) (in the x-z plane) is

$$R_t(\varphi) = \sqrt{[z-\kappa a\cos\psi]^2 + [\rho - a\kappa\sin\psi\cos\varphi]^2 + [a\kappa\sin\psi\sin\varphi]^2}\ . \tag{19}$$

The distance from ρ, z (in the x-z plane) to the feed point of the monopole is

$$R_f = \sqrt{z^2+\rho^2}. \tag{20}$$

The distance from ρ, z (in the x-z plane) to the bottom cone edge (image monopole) is

$$R_b(\varphi) = \sqrt{[z+\kappa a\cos\psi]^2 + [\rho + a\kappa\sin\psi\cos\varphi]^2 + [a\kappa\sin\psi\sin\varphi]^2}\ . \tag{21}$$

The variable $\delta_m(\varphi) = a\kappa/\left[R_t(\varphi) + R_f\right]$ is for the monopole and $\delta_i(\varphi) = a\kappa/\left[R_b(\varphi) + R_f\right]$ is for the image monopole. For the *N* wire case,

$$\varphi_j = (j - 1/2)\,\pi/N \qquad \text{with } 1 \le j \le N\,. \tag{22}$$

The scalar potential is

$$\Phi_N^{ACD}(z,\rho) = \frac{1}{4\pi\varepsilon_0\kappa a}\sum_{j=1}^{j=N}\frac{1}{N}\ln\left[\frac{\left[1+\delta_m(\varphi_j)\right]\left[1-\delta_i(\varphi_j)\right]}{\left[1-\delta_m(\varphi_j)\right]\left[1+\delta_i(\varphi_j)\right]}\right]. \tag{23}$$

The wires with $\varphi_j = -(j-1/2)\,\pi/N$ give the exact same equation as above and are not included in the calculation.

The LCD scalar potential, Equation (11), assumes the line charge is on the z-axis with a unit vector $z_j = 1$, $x_j = 0$, $y_j = 0$. The dot product of the unit vector and the field position is z. For the cone case, the unit vector for the wire in direction φ_j and ψ is $z_j = \cos\psi$, $x_j = sin(\psi)cos\varphi_j$, $y_j = sin(\psi)sin\varphi_j$.

The field position is $x = \rho\ and\ y = 0$. The projection Z_j of the field position on the φ_j wire is calculated with the dot product:

$$Z_j = z\cos\psi + \rho\sin\psi\cos\varphi_j. \tag{24}$$

The scalar potential is

$$\Phi_N^{LCD}(z,\rho) = \frac{1}{4\pi\varepsilon_0}\frac{2}{(\kappa a)^2}\sum_{j=1}^{j=N}\frac{Z_j}{N}\left[\ln\left(\frac{1+\tau(\varphi_j)}{1-\tau(\varphi_j)}\right) - 2\tau(\varphi_j)\right]. \tag{25}$$

In the general case, the error in the *N* wire numerical approximation is

$$\Phi_N^{Error}(z,\rho) = |\Phi_{3N}(z,\rho) - \Phi_N(z,\rho)|. \tag{26}$$

The $\Phi_{3N}(z,\rho)$includes the wires from $\Phi_N(z,\rho)$ plus two more wires on either side of the *N* wires. The numerical method error $\Phi_N^{Error}(z,\rho)$ is calculated to give $\Phi_N^{Error}(z,\rho)/|\Phi_{3N}(z,\rho)| \le 10^{-7}$. The exact error $\Phi_{3N}^{Error}(z,\rho)$ can only be evaluated after $\Phi_{9N}(z,\rho)$ is computed; however, the error

$$\Phi_{3N}^{Error}(z,\rho) \ll \Phi_N^{Error}(z,\rho)| \tag{27}$$

is much smaller. The leading error term can be deduced by symmetry and spherical harmonics.

The scalar potential and cone are both rotationally symmetric; however, the error in the solution has the same rotational symmetry of the 2*N* wire numerical approximation. The error is found with the spherical harmonic expansion of $\Phi_N(\theta,\phi)$. The wires are equally spaced with $\Delta\phi = \pi/N$ steps in rotational angle and they are odd in z.

The spherical harmonic term, $Y_{lm} = \sqrt{2l+1(l-m)!/4\pi(l+m)!}P_l^m(\cos\theta)e^{jm\phi}$contributes to the expansion only if it has the same rotational symmetry as the wires $m = 0,\ 2N,\ 4N,$ etc. Note: $m\Delta\phi = 2N * \pi/N = 2\pi$. The associated Legendre polynomials must be odd $P_l^m(\cos\theta) = -P_l^m(\cos(\pi-\theta))$; this limits l to odd values. The solution is the rotationally symmetric part with no $e^{jm\phi}$ dependence; the only spherical harmonic expansions contributing to the solution are $Y_{2p+1,0}/r^{2p+2}$ where $0 \le p \le \infty$.

The first error term in the spherical harmonic expansion is $Y_{2N+1,2N}/r^{2N+2}$. This term is rotationally symmetric in πN steps and odd in z. The first error term in the spherical harmonic expansion of $\Phi_{3N}(z,\rho)$ is $Y_{6N+1,6N}/r^{6N+2}$. At large distances, the largest error is proportional to

$$\Phi_N^{Error}(z,\rho) \propto |Y_{2N+1,2N}/r^{2N+2}|. \tag{28}$$

This numerical method converges very fast with the sequence *N*, 3*N*, 9*N*, etc. The ACD and LCD scalar potentials are combined with the coefficients from Equation (2):

$$\Phi_N^{UWB}(z,\rho) = (1-\alpha)\,\Phi_N^{ACD}(z,\rho) + \alpha\Phi_N^{LCD}(z,\rho). \tag{29}$$

The capacitance is computed from

$$\Phi_{Max}^{UWB}(\kappa,\psi) = \max\left[\Phi_N^{UWB}(z_{Sphere},\rho_{Sphere})\right], \tag{30}$$

where $z_{Sphere} = a\cos\theta$, $\rho_{Sphere} = a\sin\theta$ and θ is measured from the z-axis and $0 \le \theta \le \pi/2$.

The capacitance is

$$C^{UWB}(\kappa,\psi) = q_{Total}/\Phi_{Max}^{UWB}(\kappa,\psi). \tag{31}$$

Note: the charge distribution is defined to give $q_{Total} = 1$, Equation (6). Figure 5 is the capacitance/a as a function of the cone geometry ψ and κ. The capacitance is scaled by *1/a* to make the design curve independent of the enclosing sphere's radius a. For a fixed ψ, increasing κ moves the charge distribution cone closer to the enclosing sphere; this increases the peak scalar potential and decreases capacitance. For a fixed κ, the larger half cone angle ψ increases the distance between the enclosing sphere and the charge distribution on the cone. This decreases the peak scalar potential on the enclosing sphere. The negative charge on the image cone is also closer to the top part of the enclosing sphere; this also reduces the peak scalar potential. The peak scalar potential on the enclosing sphere is significantly reduced for the higher half cone angles; this increases the capacitance. In Figure 5, the distance between contours is smaller for the larger values of ψ.

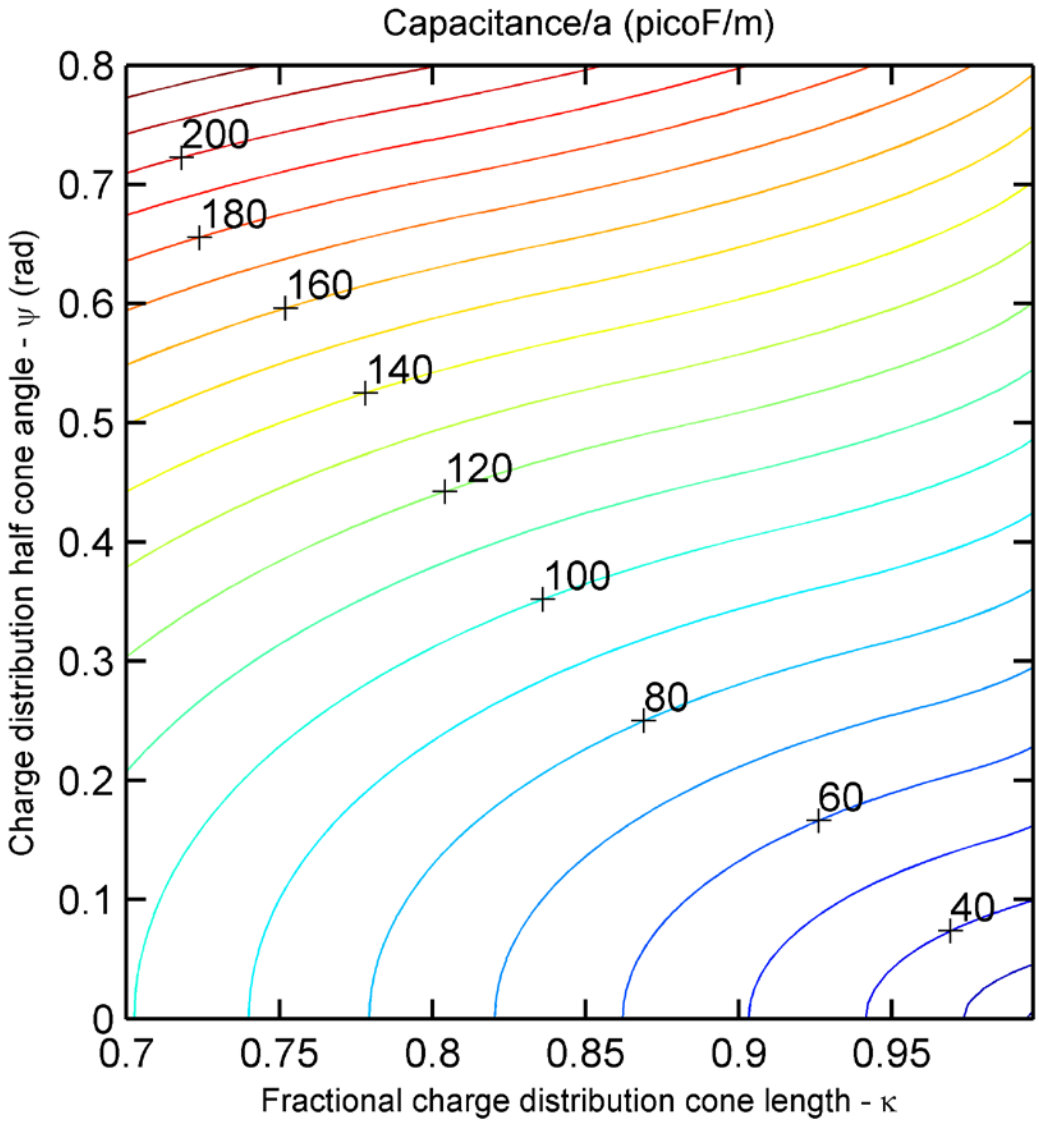

Figure 5. Capacitance design curve as function of the charge distribution geometry κ and ψ, which is computed from the potential on the antenna and net charge on dipole arm.

4. UWB ANTENNA Q-FACTOR RATIO

The capacitance and radiation resistance are combined to compute the Q-factor ratio as a function of fractional charge-distribution-cone length and charge-distribution-cone half angle ψ. Only a subset of solutions representing an antenna with a conical feed point will be considered. Other solutions with non-conical feed points may not be UWB. The value $\alpha = 0.35$ is selected for the 50-Ω input impedance antenna design; it is a good approximation of the feed point cone for the other design in the paper. The accuracy of the feed point cone is critical to the calculation of the capacitance$/a$, radiation resistance$/(ka)^2$, and Q-factor ratio. In the following plots, the antenna design curves are independent of frequency and enclosing sphere's radius a. The Q-factor ratio is valid in the limit as frequencies $f \rightarrow 0$.

Figure 6 plots Q-factor ratio, $Q*(ka)^3$, as a function of the cone geometry κ and ψ. For small ψ, the minimum Q-factor ratio has moderate κ values. For large ψ, the Q-factor ratio has high κ values. The transition region is expanded in Figure 7; there is an absolute minimum and a local minimum for some values of ψ. The absolute and a local minimum are the same at $\psi = 0.19481$; the absolute minimum shifts from $\kappa \sim 0.84$ to $\kappa \sim 0.98$.

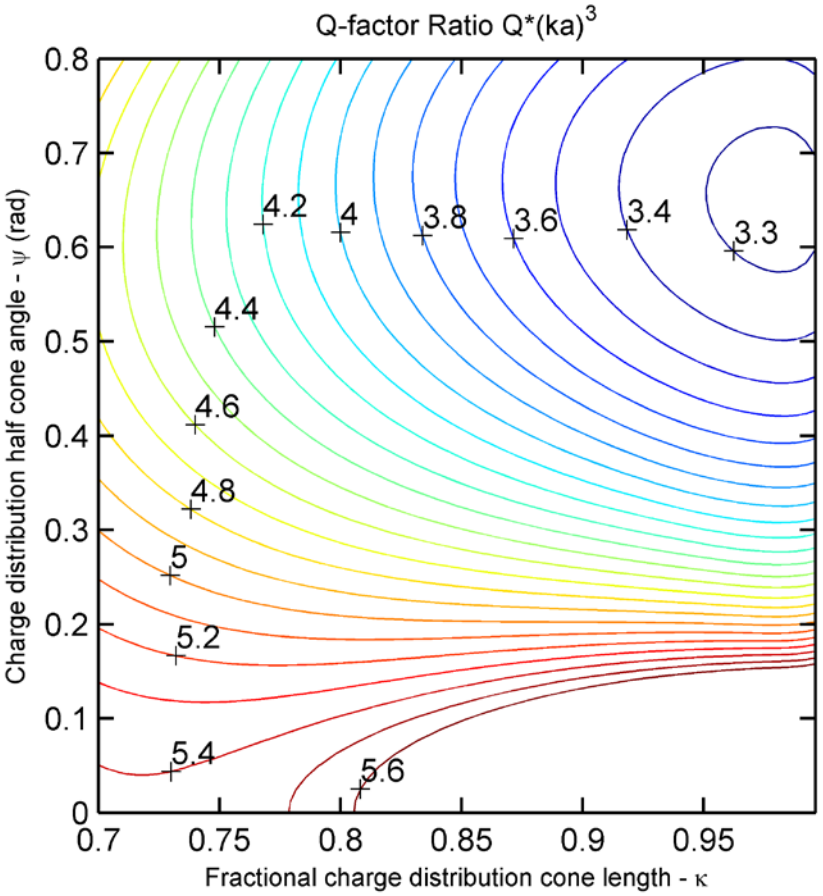

Figure 6. The Q-factor ratio design curve as function of the charge distribution geometry κ and ψ. The Q-factor ratio design curve is computed from the radiation resistance and capacitance.

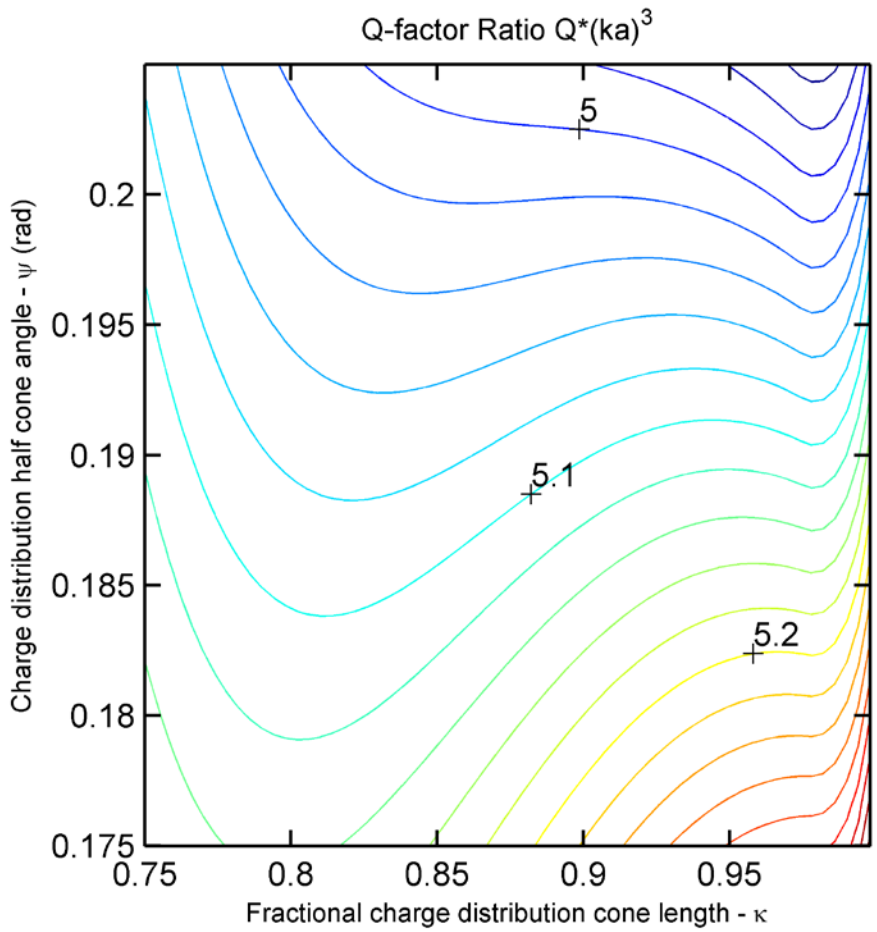

Figure 7. The Q-factor radio has an absolute minimum and a local minimum for a range of cone geometries κ and ψ. As ψ increases, the absolute minimum shifts from $\kappa \tilde{} 0.84$ to $\kappa \tilde{} 0.98$.

Figure 8 plots the minimum Q-factor ratio, $Q * (ka)^3$, as a function of Ψ in radians; the capacitance, C/a; radiation resistance, $R_{Rad}/(ka)^2$; and 10κ for this solution are also plotted. At the discontinuity, Q-factor ratio has the same values at two point with different values of κ. Below the discontinuity, the increasing κ in turn increases $R_{Rad}/(ka)^2$ and also increases the scalar potential on the sphere, which reduces the capacitance of the antenna. Above the discontinuity, κ is almost a constant, $R_{Rad}/(ka)^2$ decreases with the $cos^2\Psi$. The capacitance increases with the charge-distribution-cone half angle Ψ. The surface charge density is spread over a much larger surface area, which reduces the peak scalar potential on the enclosing sphere and increases the capacitance. For $\Psi > 0.177$, the minimum Q-factor antenna no longer touches the top of the enclosing sphere. For charge-cone half angles $0.195 \leq \Psi \leq 0.715$ range, κ is constant.

The first row in Table 1 is the minimum Q-factor ratio for the line charge distribution. The last two rows in Table 1 have similar input impedance but very different shapes. Figure 9 plots the line-charge-distribution Q-factor ratio design curve as a function of κ. Figure 10 plots the antenna shape for the ICC antenna and the minimum Q-factor-ratio, line-charge-distribution design. The line-charge-distribution bulb shape is almost the same as the ICC antenna, but the ICC feed point cone is much smaller. The 50- Ω input impedance ICC antenna will be used as the best existing solution. Simpson, Pavlovic, and Olcan [13] did not evaluate the ICC antenna for different cone half angles; the 50- Ω input impedance ICC antenna may not be the minimum Q-factor solution.

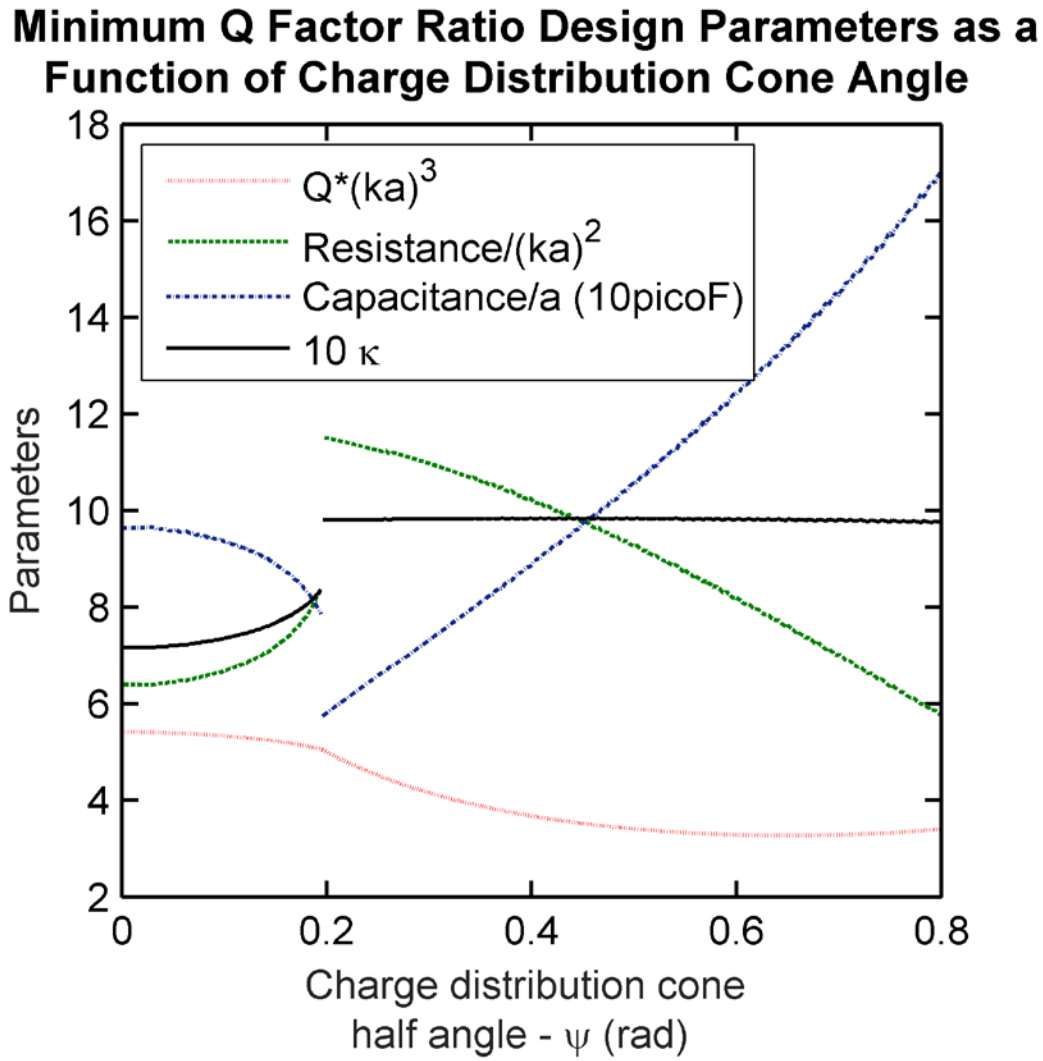

Figure 8. The minimum Q-factor ratio, capacitance/a, $10\,\kappa$, and resistance/$(ka)^2$ as a function of ψ. At the discontinuity, the Q-factor ratio has the same value at two different points; see Figure 7 and Figure 11.

The second row in Table 1 is the maximum resistance design. Figure 11 plots Q-factor-ratio design curves for $\psi = 0.1946$, $\psi = 0.19481$, and $\psi = 0.195$. The minimum Q shifts from $\kappa \sim 0.84$ on the $\psi = 0.1946$ design curve to $\kappa \sim 0.98$ on the $\psi = 0.195$ design curve. The design curve for $\psi = 0.19481$ has two equal minimum Q-factor-ratios. The maximum R_{Rad} design does not give a significant decrease in Q-factor ratio and will not be numerically modeled.

Row 3 in Table 1 is 50-Ω input impedance design. The parameters are selected to touch the enclosing sphere at the top. The 50-Ω input impedance design curve, Figure 12, shows the minimum Q-factor ratio and the position of the design. Figure 13 is the 50-Ω input impedance design cross section that fills the top of the sphere. Figure 14 shows that the antenna design is a very good approximation of the 50-Ω input impedance cone.

The last two rows in Table 1 have similar input impedance but very different shapes. A 30-input impedance design touches the top of the enclosing sphere. On the other hand, the 32-minimum Q-factor-ratio design touches the side of the enclosing sphere. Figure 15 shows the two design curves for fixed $\psi = 0.5296$ and $\psi = 0.653$. There is a significant difference on the Q-factor ratios of the two antennas. Figure 16 shows there is a significant difference in the antenna shape. The next section shows that the 32-input impedance design reduces the lowest operational frequency without increasing the VSWR at higher frequencies.

Table 1. Antenna design parameters: radiation resistance/$(ka)^2$, capacitance, and Q-factor ratio.

Parameter	ψ	κ	$R_{Rad}/(ka)^2$	C/a	$Q^*(ka)^3$
Line charge	0	0.7150	6.3747	96.6077 ρF	5.413
Max R_{Rad}	0.1948	0.9789	11.5	57.45 ρF	5.045
50 Ω	0.3408	0.940	9.7871	84.9754 ρF	4.008
30 Ω	0.5296	0.8711	7.047	127.805 ρF	3.701
Min. Ω factor ratio 32 Ω	0.653	0.9809	7.5688	134.890 ρF	3.265

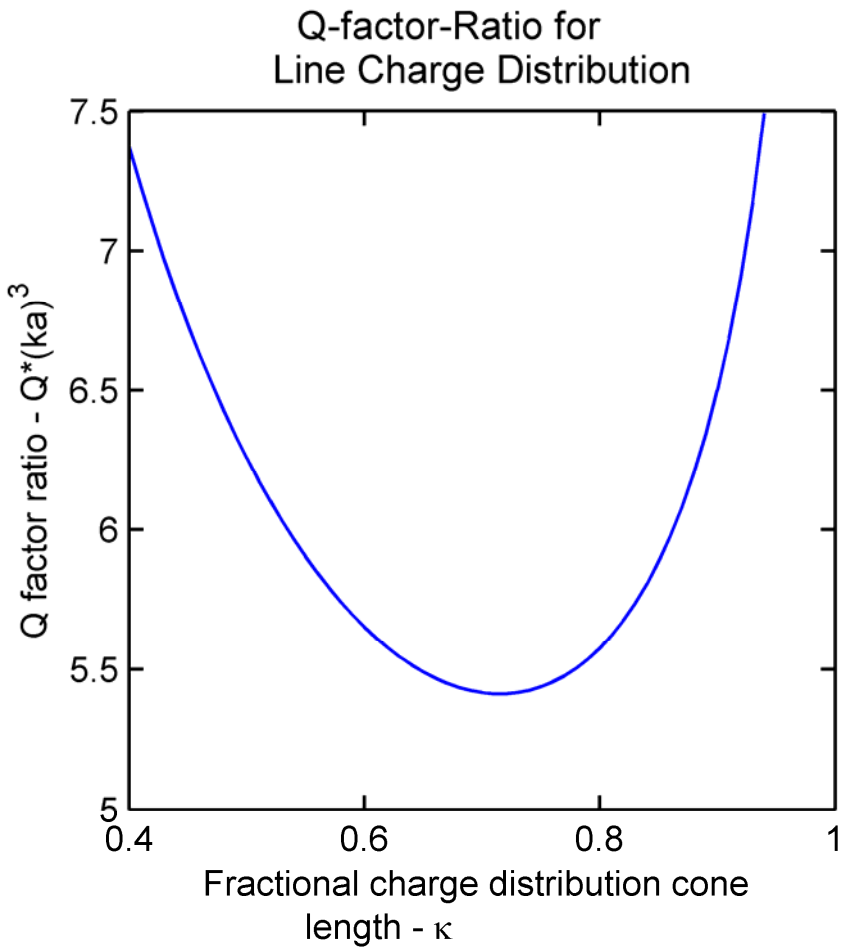

Figure 9. Q-factor ratio for the z-axis line charge distribution as a function of κ with $\psi = 0$.

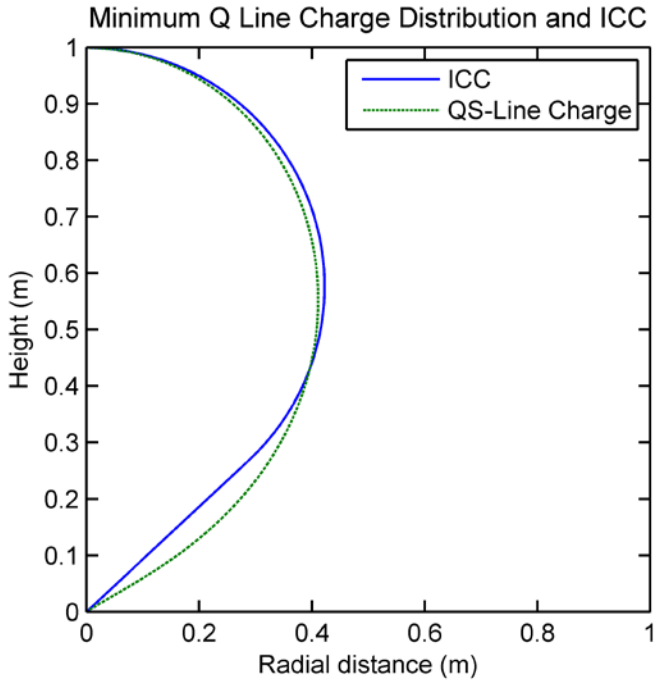

Figure 10. The 50-Ω input impedance ICC and the minimum Q line charge distribution designs ($\psi = 0$).

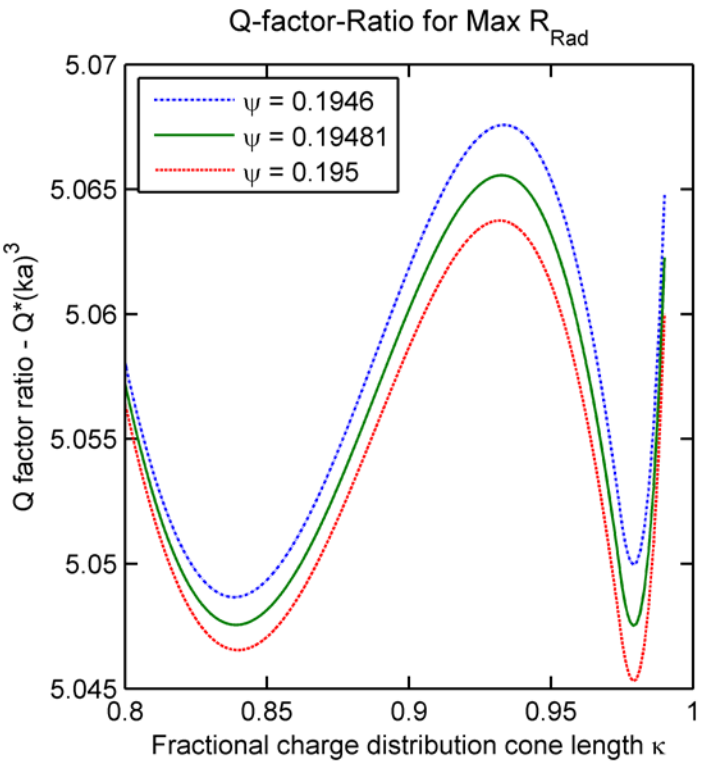

Figure 11. The κ of the minimum Q shifts from 0.84 to 0.979. This significantly increases the R_{Rad} without changing Q.

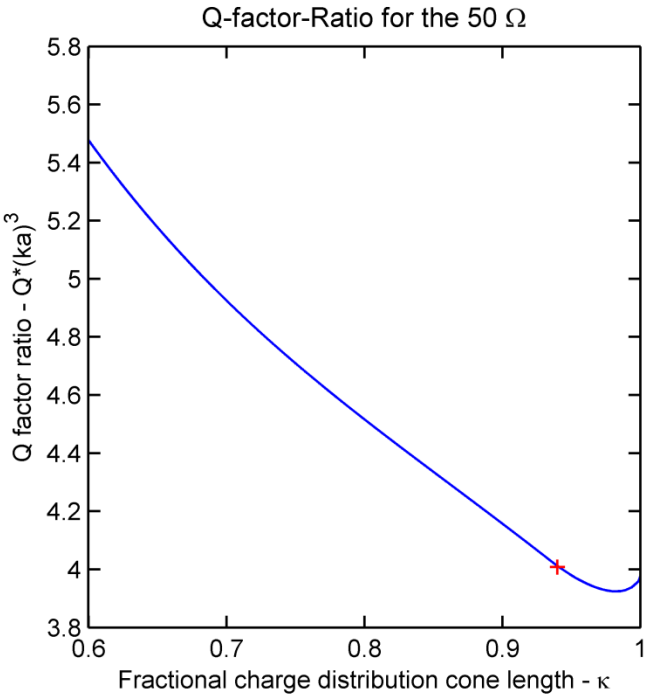

Figure 12. The *Q*-factor ratio design curve for charge distribution cone geometry $\psi = 0.3408$ and κ. The design, marked with "+", touches the top of the sphere.

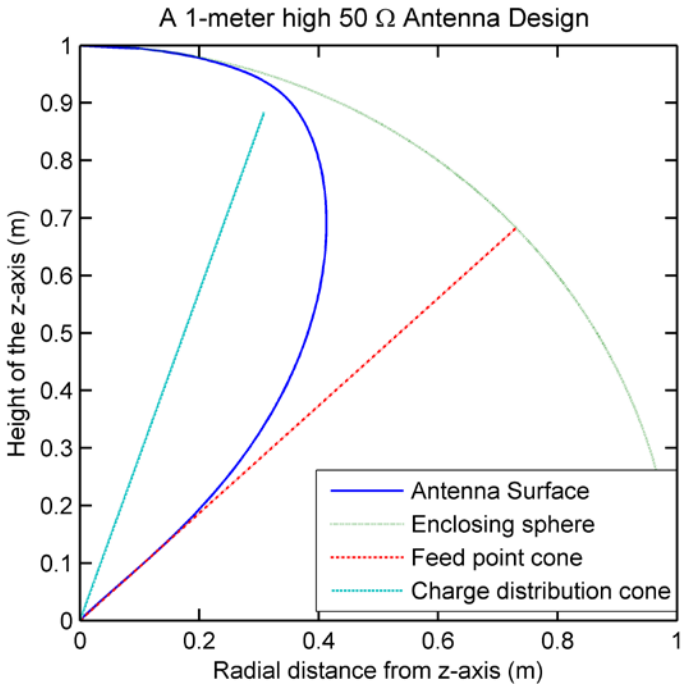

Figure 13. The enclosing sphere, antenna shape, feed point cone angle, and charge distribution cone.

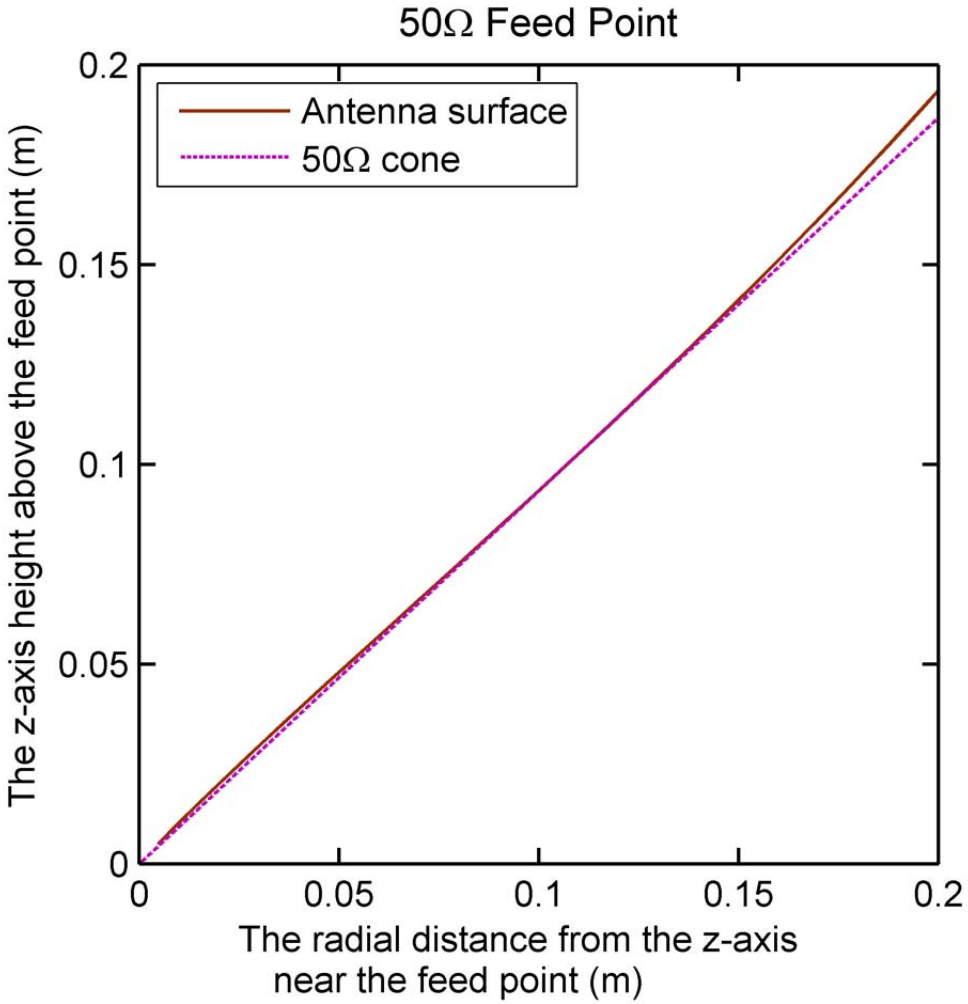

Figure 14. The antenna shape is a very good approximation of the 50-Ω cone.

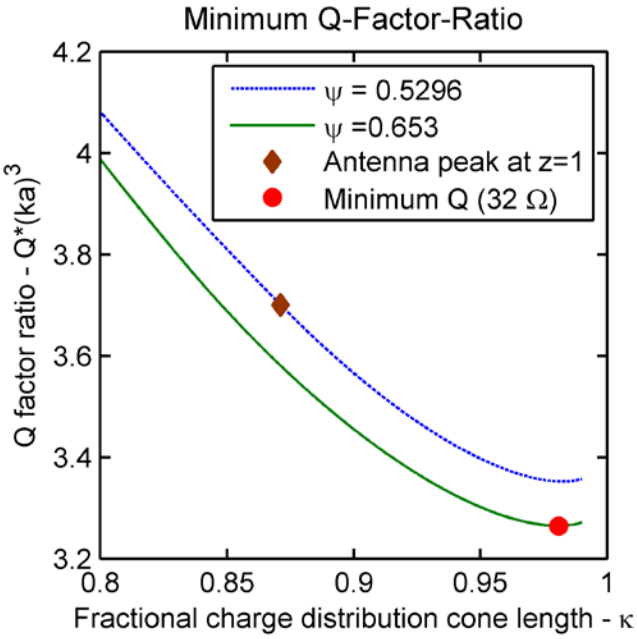

Figure 15. The Q-factor ratio is significantly higher for the antenna that touched the top of the enclosing sphere, $\psi = 0.5296$. The design that touched the side of the enclosing sphere has a lower Q-factor ratio, $\psi = 0.653$.

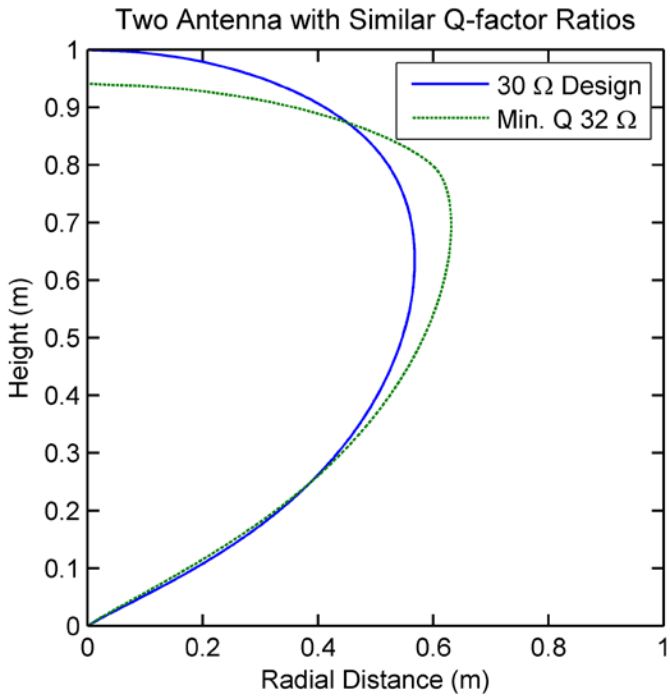

Figure 16. The green antenna has a lower Q-factor ratio than the blue antenna. The higher curvature on the green antenna does not influence the VSWR of the antenna, see Figure 27.

5. NUMERICAL RESULTS

The numerical results are calculated with the T-solver in Computer Simulation Technology (CST) Microwave Studio®. The numerical model uses a coaxial cable (source) embedded in a thin cone 6 mm high with a diameter of 400 mm on the ground plane. For the 50-Ω coaxial source, the inner conductor is 6 mm radius wire and the outer conductor is 13.8 mm in radius. Air is the insulator between the conductors. The coaxial inner conductor extends into the body of the antenna replacing the point of the cone with a cylinder. The problem size is reduced by using $B = 0$ on the x-z and y-z symmetry plane. Energy adaptation was used to obtain a series of mesh refinements. In the initial work, the antennas were selected to touch the top of the sphere, $\rho = 0$ and $z = 1$.

Figure 17 is the cross section of the CST antenna model for the 50-Ω input impedance antenna. Figure 18 is the Smith chart and Figure 19 is the VSWR plot for the frequency range 30 MHz to 2.5 GHz. The VSWR is 2:1 at 54.813 MHz; this is an 8.6% reduction in size compared to the results of Simpson, Pavlovic, and Olcan [13]. The VSWR is less than 1.2:1 for nearly all of the frequency range. This is an unexpected result.

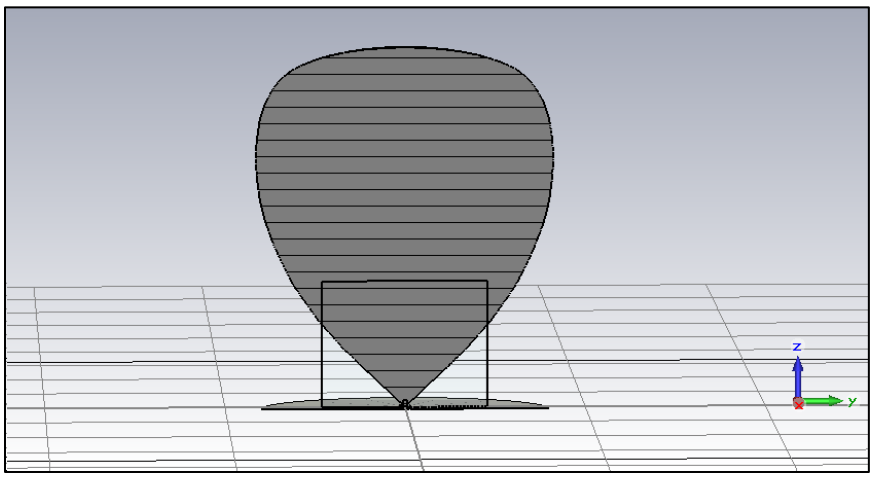

Figure 17. A cross section of the CST 50-Ω input impedance 1-meter-high monopole.

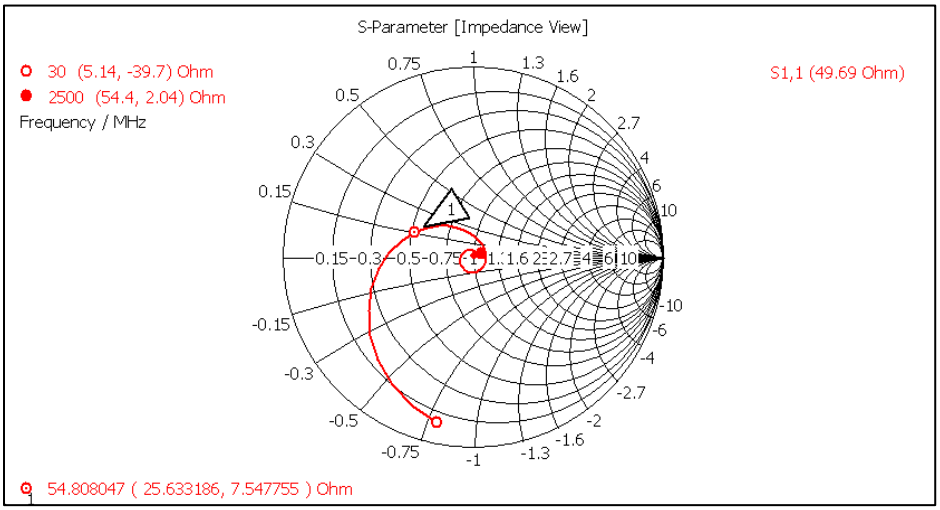

Figure 18. The Smith chart for the 1-meter-high 50-Ω input impedance monopole.

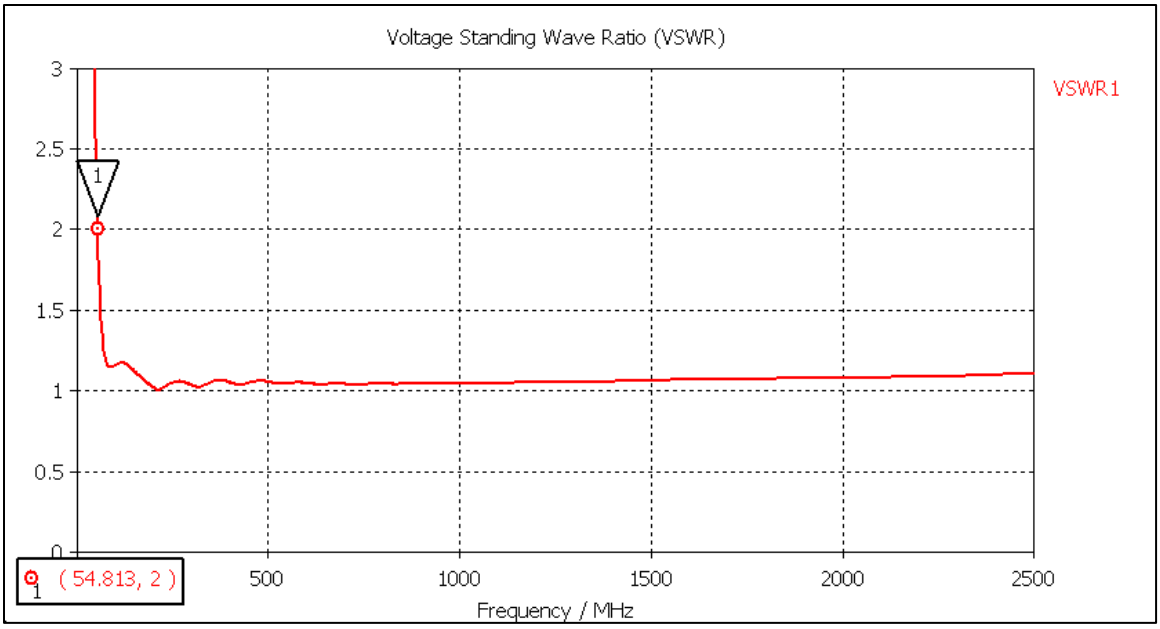

Figure 19. The VSWR for the 1-meter-high 50-Ω input impedance monopole.

The Q-factor and lowest operating frequency can be reduced by increasing charge-distribution-cone half angle ψ; this lowers the impedance of the feed-point cone and increases the capacitance. The numerical model uses a 30-Ω coaxial source embedded in a thin-cone 3 mm high with a diameter of 400 mm on the ground plane. For the 30-Ω coaxial source, the inner conductor is 3 mm in radius wire and the outer conductor is 5.001 mm in radius. Air is the insulator between the conductors. The coaxial inner conductor extends into the body of the antenna replacing the point of the cone with a cylinder. Energy adaptation was used to obtain a series of mesh sizes. This antenna touches the top of the sphere, $\rho = 0$ and $z = 1$.

Figure 20 is the cross section of the CST antenna model for the 30-Ω input impedance antenna. Figure 21 is the Smith chart and Figure 22 is the magnitude of the reflection coefficient, Γ for the frequency range 20 MHz to 2.5 GHz. The VSWR is 2:1 at 48.9 MHz or $\lambda/6.134$. This is almost a 18.5% reduction in size compared to Simpson, Pavlovic, and Olcan's [13] results. The reflection coefficient ranges from 1/10 to 1/20 for nearly all of the frequency range (VSWR 1.2 to 1.1). Figure 23 is the CST source pulse and Figure 24 is the CST reflected pulse. Note: the scale on the reflected pulse is 4% of source pulse. At the feed point, the reflection is 3.9% of the incident pulse.

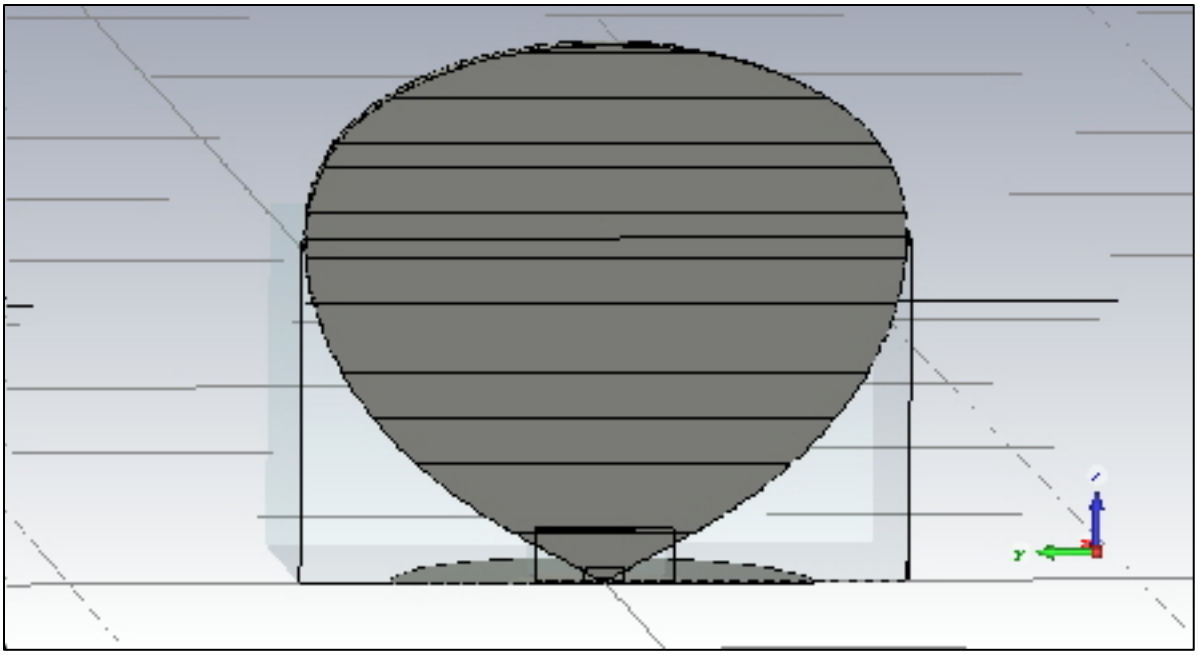

Figure 20. The1-meter-high 30-Ω input impedance UWB antenna design that touches the top of the sphere.

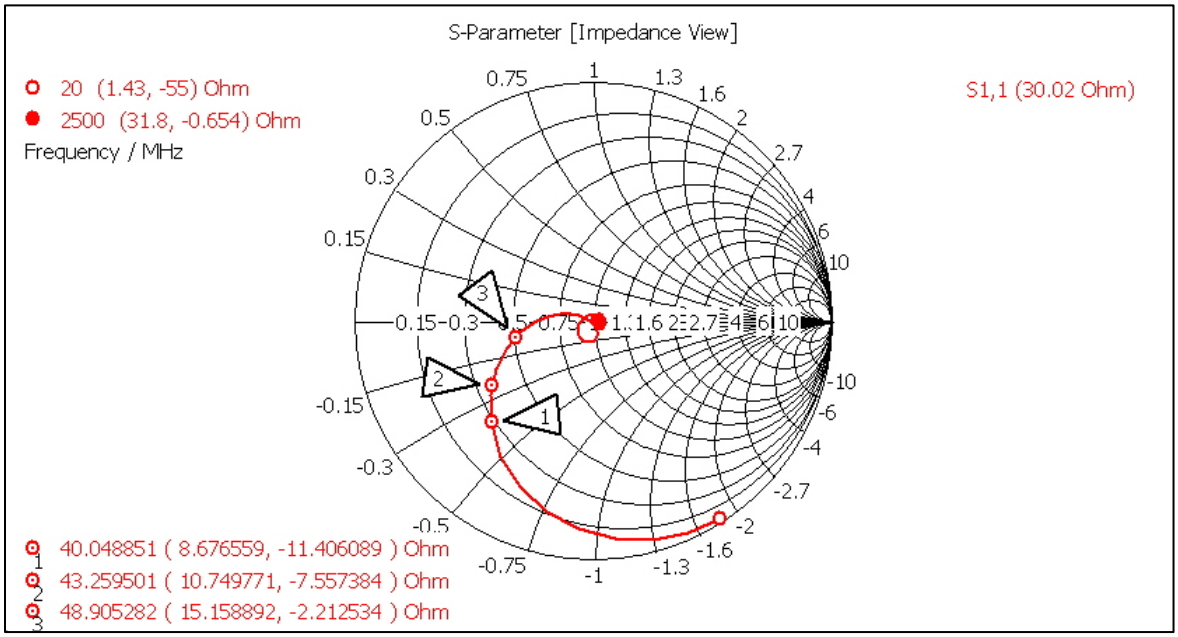

Figure 21. The Smith chart for 30-Ω input impedance antenna that touches the top of the sphere.

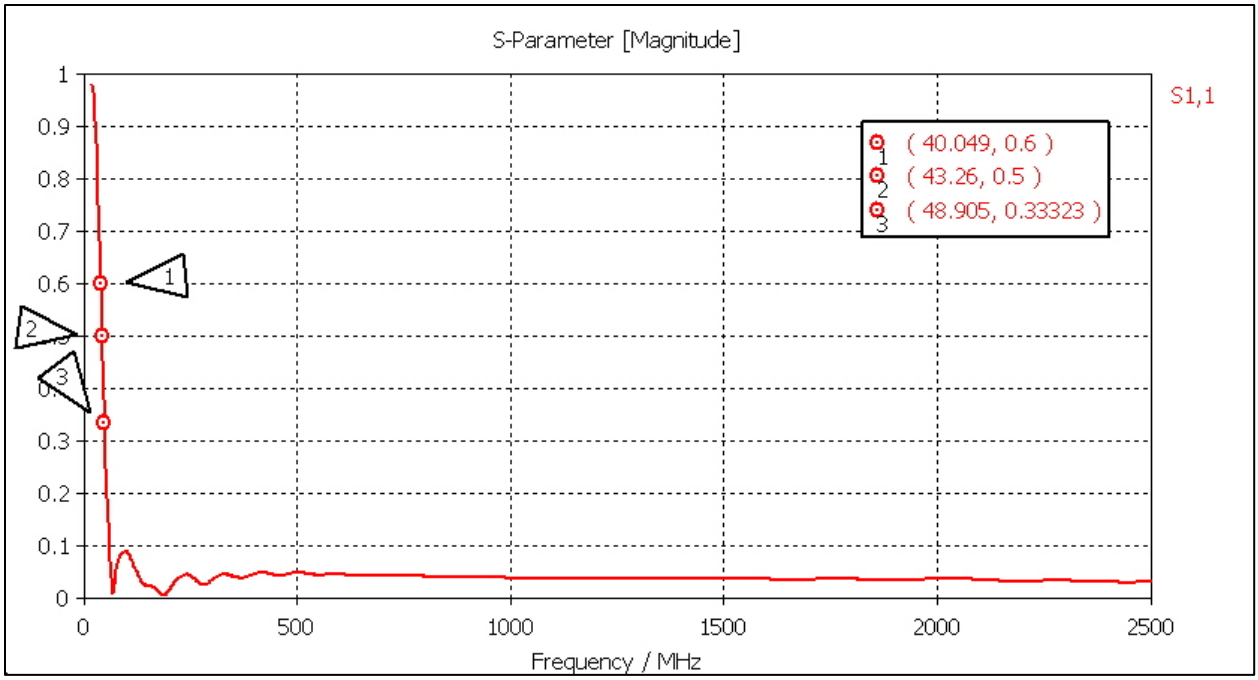

Figure 22. The CST frequency domain reflection coefficient for the 30-Ω input impedance antenna that touches the top of the sphere. The VSWR 4:1, 3:1, and 2:1 are labeled as 1, 2, and 3, respectively.

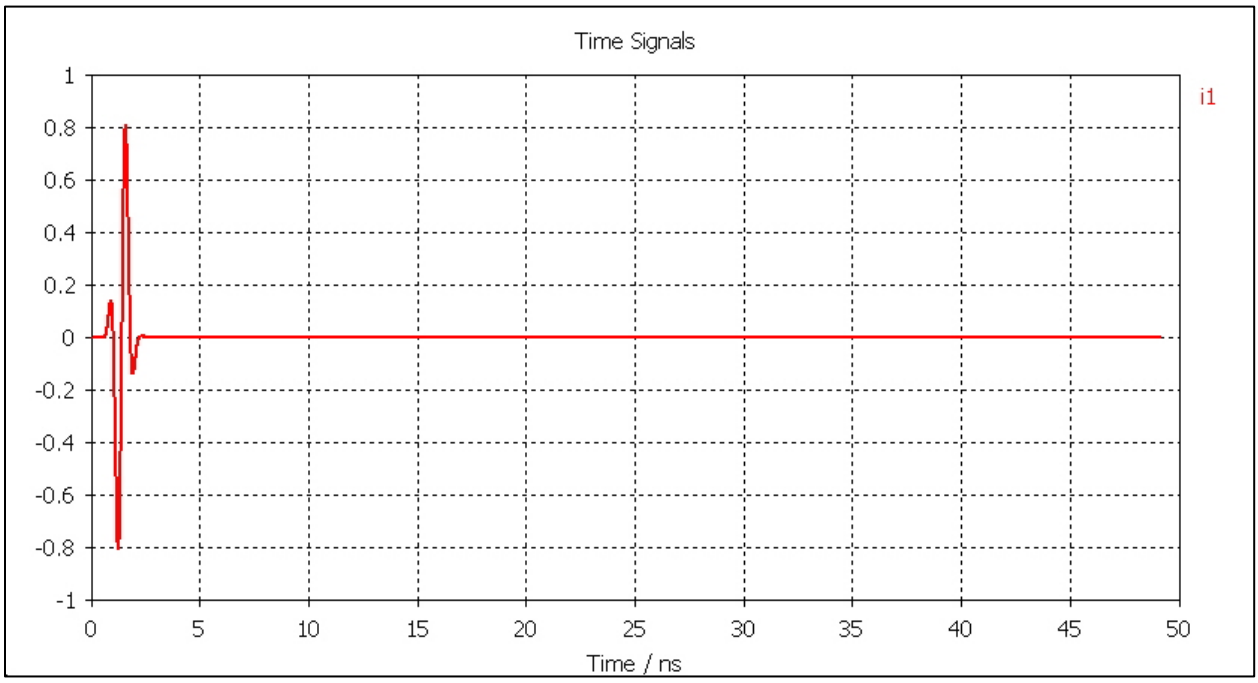

Figure 23. The CST source pulse for 30-Ω input impedance antenna that touches the top of the sphere.

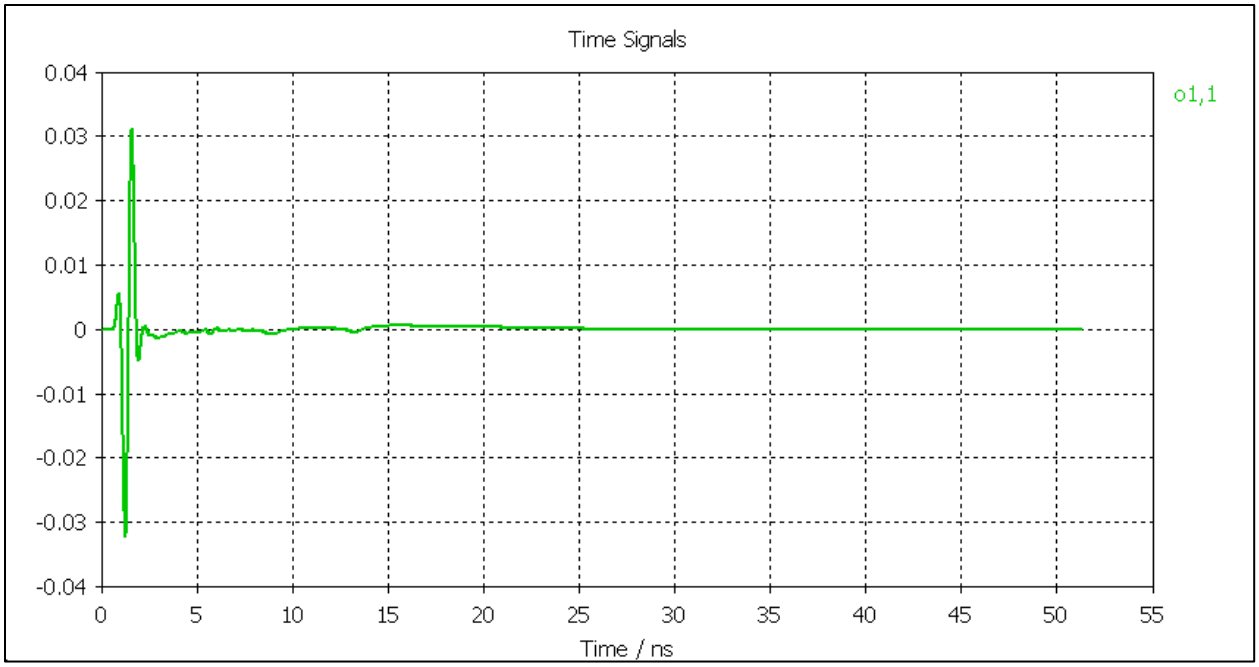

Figure 24. The CST pulse reflected from the feed point for 30-Ω input impedance antenna that touches the top of the sphere.

The final design places no restriction on the antenna shape. The top of the antenna no longer touches the top of the sphere. Figure 25 is the cross section of the CST antenna model for the 32-Ω input impedance antenna. Figure 26 is the Smith chart and Figure 27 is the VSWR plot for the frequency range of 20 MHz to 2.5 GHz. The VSWR is 2:1 at 48.9 MHz, which is slightly larger than the previous result. The VSWR is less than 1.2:1 for nearly all of the frequency range. Figures 28 and 29 are the CST source and reflected pulse. Note: the scale on the reflected pulse is 4% of source pulse. At the feed point, the reflection is 3.9% of the incident pulse. In Figure 16, the minimum Q antenna design has a rapid change in curvature near the enclosing sphere. One would expect RF to be reflected from this region, but the RF is not reflected, which implies that other changes in shape can be made without increasing the VSWR. The antennas capacitance and radiation resistance can both be increased and Q-factor decreased by filling the top of the sphere. A more complex charge distribution model can be used to extend the cone length, fill the top of the sphere, and significantly reduce the Q-factor.

Table 2 summarizes the VSWR numbers for the three designs. The frequencies for 3 to 1 and 4 to 1 VSWR are steadily decreasing with lower Q. Hujanen, Holmberg, and Sten [17] calculated the smallest possible *ka* value for the UWB antenna size and VSWR. This analytic solution assumes a dipole mode with an infinite lossless matching network. The UWB antenna size is $ka \geq 0.46833$ or $a = \lambda_{max}/13.4$ for a 3:1 VSWR. They pointed out that an antenna can be "pre-tuned" and not require a matching network. Their derivation does not indicate the size of a pre-tuned antenna. Yang, Davis, and Stutzman [18] designed an antenna with a 10:1 bandwidth and an antenna size $a = \lambda_{max}/8$.

Table 2. Lowest operating Frequency for Different VSWRs.

Design	$Q*(ka)^3$	$\rho = 1/3$	2:1 VSWR	3:1 VSWR	4:1 VSWR
50 Ω	4.008	1.149 ka	54.81 MHz	47.18 MHz	43.08 MHz
30 Ω	3.701	1.006 ka	48.005 MHz	43.23 MHz	40.05 MHz
Min. Q factor ratio 32 Ω	3.265	1.025 ka	48.90 MHz	42.67 MHz	39.25 MHz

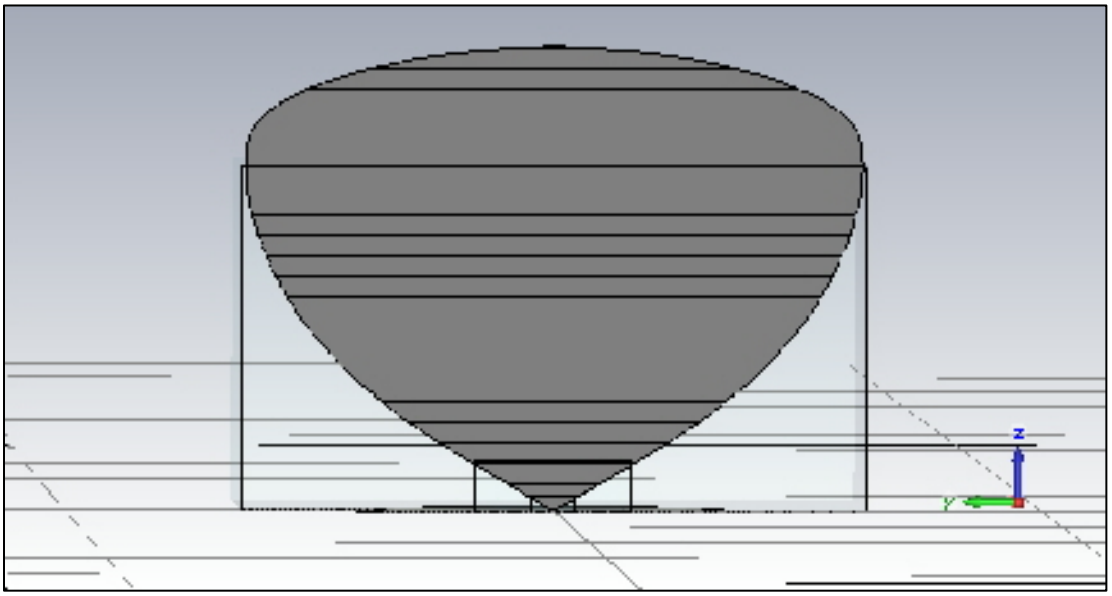

Figure 25. Minimum Q-factor design computed from the QSADA. The antenna does not fill the top of the sphere.

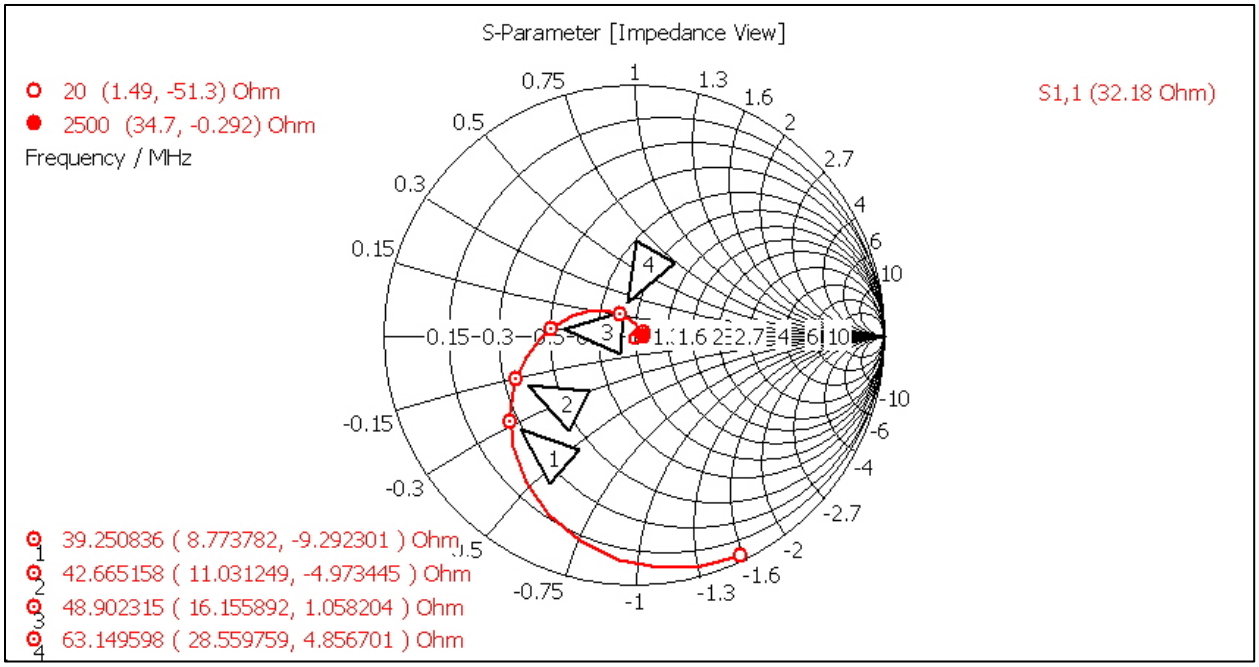

Figure 26. Smith chart for the minimum Q-factor design computed from the QSADA. The VSWR 4:1, 3:1, 2:1, and 1.14:1 are labeled by 1, 2, 3, and 4, respectively.

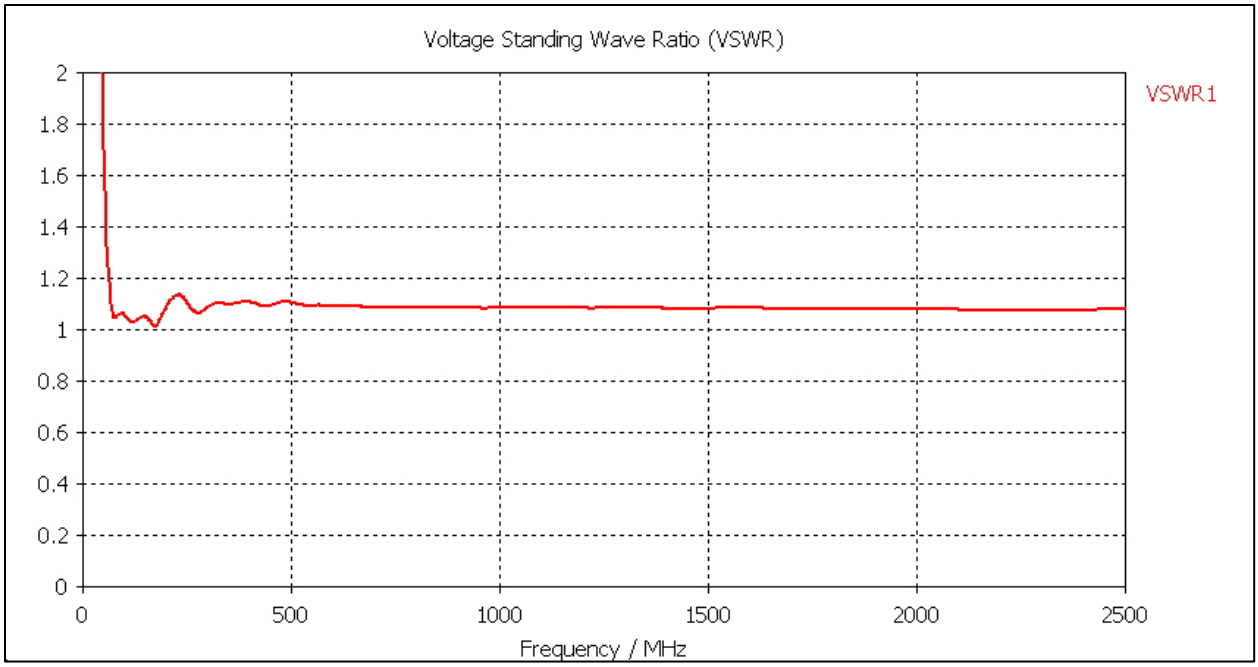

Figure 27. VSWR for the minimum Q-factor design CST model.

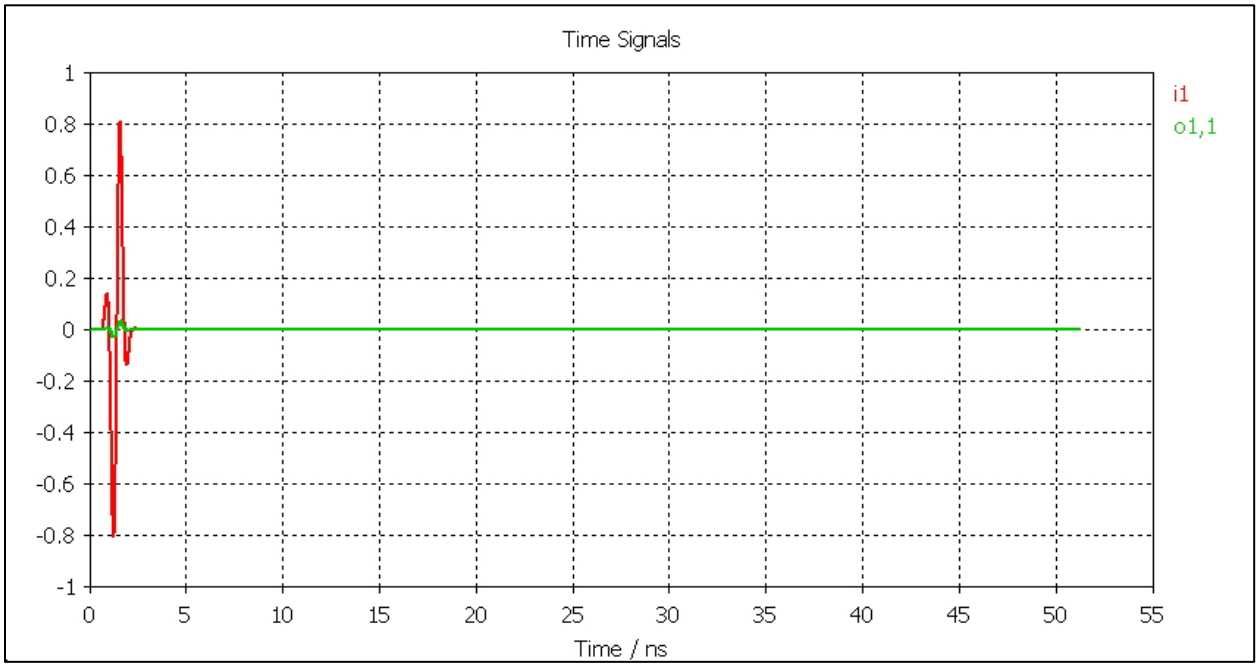

Figure 28. The CST source pulse (red) and reflection (green) for the minimum Q-factor design computed from the QSADA.

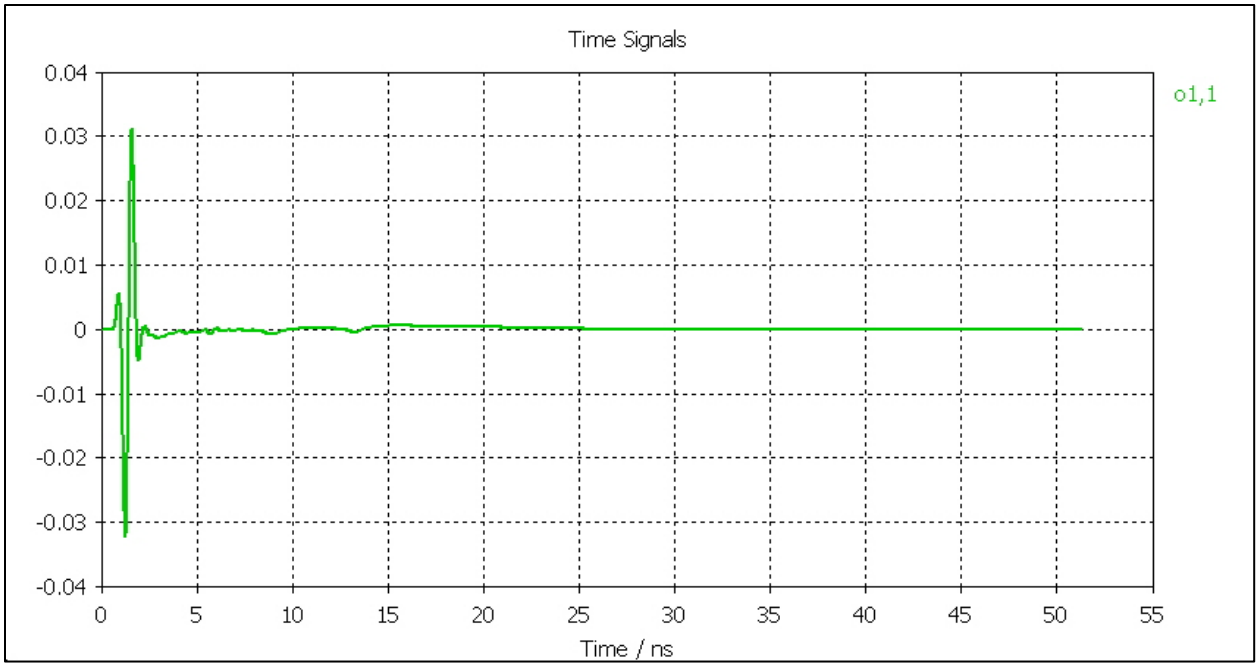

Figure 29. The CST reflection from the feed point for the minimum Q-factor design computed from the QSADA.

6. CONCLUSION

The Quasi-static Antenna Design Algorithm is a general method for designing cylindrically symmetric antenna. This report covers the UWB antenna design and [6] discusses the electrically small antenna design. The general top load [6] can be added to the conical charge distribution to model more complex charge distributions.

The Quasi-static Antenna Design Algorithm is a physics-based approach for UWB antenna designs. The cone with a bulb shape is used as a UWB antenna model. Minimizing the Q-factor ratio for this model yields cone and bulb shapes with improved low-frequency performance. The lowest Q-factor ratio is a 32-Ω input impedance UWB antenna that fills most of the enclosing sphere's volume. The 30-Ω input impedance and minimum Q-factor ratio designs have very different shapes with similar Q-factor ratios and very low VSWR, as shown in Figure 16. The shape difference should reflect RF back to the feed point; this is an unexpected result. One would expect that the VSWR to increase as the operating frequency is reduced. The lowest operating frequency of the UWB antenna should give a uniform VSWR over the entire band. Any further reduction in operating frequency would reduce the antenna bandwidth.

The above model uses a linear charge distribution on the cone. The quasi-static antenna design algorithm can use a sequence of more complex charge distribution models: quadratic, cubic, etc., on the cone. Each new charge distribution should extend the length on the cone and the size of the bulb, which moves the charge distribution to a higher position on the antenna, increasing the effective height and radiation resistance. The larger cone and bulb will also reduce the surface-charge density on the antenna, which reduces the electric field around the antenna and increases the capacitance. Both factors reduced the Q. Each minimum Q-factor design requires numerical modeling to evaluate the impedance and the VSWR. The quasi-static antenna design algorithm will reduce the lowest operating frequency of the antenna; however, the new antenna shape could adversely impact the high frequency response of the antenna. The Q-factor design curves allow the antenna shape to be modified by selecting a new design near the minimum Q factor ratio. This could round the bulb shape and reduce VSWR. The Quasi-static Antenna Design Algorithm should be able to design significantly smaller UWB antennas.

REFERENCES

1. De, N. C., T. K. Ghosh, D. P. Poddar, and S. K. Chowdhury. 1995. “Design and Experimental Investigation of the Asymptotic Conical Dipole Antenna,” *IEEE Transactions on Electromagnetic Compatibility*, vol. 37. no. 2 (May), pp. 282–285..
2. Jones III, T. O. 2011. “A Quasi-Static Design Antenna Design Approach for Minimum-Q Antennas,” *IEEE Antenna and Propagation Magazine*, vol. 53, no. 3 (June), pp. 84–94.
3. Jones III, T. O. 2012. “Quasi-Static Design Approach for Minimizing the Quality Factor 'Q for Electrically Small Antennas. U.S. Patent 8,121,821 B1. February 21.
4. Jones III, T. O. 2013. “Dipole Moment Term for an Electrically Small Antennas.” U.S. Patent 8,368,156 B1. February 5, 2013.
5. Jones III, T. O. 2013. “Convergence of the Quasi-Static Design Antenna Design Algorithm.”, Technical Document 2016 (April). Space and Naval Warfare Systems Center Pacific San Diego (SSC SD), San Diego, CA.
6. Jones III, T. O. 2015. “Quasi-Static Antenna Design Algorithm: A Scientific Approach to Designing Electrically Small Antennas,” *IEEE Antenna and Propagation Magazine*, vol. 57, no. 5 (October), pp, 94–106.
7. Chu, L. J. 1948. “Physical Limitations of Omnidirectional Antennas,” *Journal of Applied Physics*, vol. 19, no. 12 (December), pp. 1163–1175.
8. Schantz, J. 2005. *The Art and Science of Ultrawideband Antennas*. Artech House, Boston, MA.
9. Lodge, O.. 1898. “Electric Telegraphy.” Patent 609, 154, August 16.
10. Sergei, A. Schelkunoff and Harald Friis. 1952. *Antennas: Theory and Practice*, pp. 317–318. John Wiley and Sons, New York, NY.
11. Paulsen, L., J. B. West, W. F. Perger, and J. Kraus. 2003. “Recent Investigation of Volcano and Smoke Antenna.” *Proceedings of the IEEE Antenna and Propagation Society International Symposium, Volume 3* (pp. 845–848). June 22–27, Columbus, OH.
12. Maloney, J. G., and G. S. Smith. 1993. “Optimization of a Conical Antenna for Pulse Radiation: An Efficient Design Using Resistive Loading,” *IEEE Transactions on Antennas and Propagation*, vol. 41, no. 7 (July), pp. 940–947.
13. T. Simpson, M. Pavlovic, and D. Olcan. 2011. “Comparing Pulse Radiation from Unloaded Ice Cream Cone and Resistively Loaded Cone.” *Proceedings of the IEEE International Symposium on Antenna and Propagation (APSURSI)* (pp. 3309–3312). July 3–8, Spokane, WA.
14. Simonds, H. B. 2003. “Compact Broad Band Antenna.” US 6,667,721 B1. December 23.
15. Jones III, T. O. 2016. “Ultra-Wideband Antenna with Conical Feed Structure and Hyperbolic Cosine Taper.” U. S. Patent 9252495. February 2.
16. Jones III, T. O. 1994. “Convergence and Error Estimation in the Method of Moments.” Technical Document 2566 (May). NRaD (now Space and Naval Warfare Systems Center Pacific), San Diego, CA.
17. Hujanen, A., J. Holmberg, and J. C.-E. Sten. 2005. “Bandwidth Limitations of Impedance Matched Ideal Dipole,” *IEEE Transactions on Antennas and Propagation*, vol. 53 (October), pp. 3236–3239.

18. Yang, T., W. A. Davis, and W. L. Stutzman. 2008. “The Design of Ultra-Wideband Antennas with Performance Close to the Fundamental Limits.” URSI, France.

REPORT DOCUMENTATION PAGE

Form Approved
OMB No. 0704-01-0188

PLEASE DO NOT RETURN YOUR FORM TO THE ABOVE ADDRESS.

1. REPORT DATE *(DD-MM-YYYY)*	**2. REPORT TYPE**	**3. DATES COVERED** *(From - To)*
February 2017	Final	

4. TITLE AND SUBTITLE

Quasi-static Design of Electrically Small Ultra Wideband Antennas

5a. CONTRACT NUMBER

5b. GRANT NUMBER

5c. PROGRAM ELEMENT NUMBER

6. AUTHORS

Thomas O. Jones III

5d. PROJECT NUMBER

5e. TASK NUMBER

5f. WORK UNIT NUMBER

7. PERFORMING ORGANIZATION NAME(S) AND ADDRESS(ES)

SSC Pacific
53560 Hull Street
San Diego, CA 92152–5001

8. PERFORMING ORGANIZATION REPORT NUMBER

TR 3056

9. SPONSORING/MONITORING AGENCY NAME(S) AND ADDRESS(ES)

SSC Pacific
53560 Hull Street
San Diego, CA 92152–5001

10. SPONSOR/MONITOR'S ACRONYM(S)

SSC Pacific

11. SPONSOR/MONITOR'S REPORT NUMBER(S)

12. DISTRIBUTION/AVAILABILITY STATEMENT

Approved for public release.

13. SUPPLEMENTARY NOTES

14. ABSTRACT

The ultra wideband (UWB) antenna shape determines both the lowest operating frequency and *Q*-factor ratio. For electrically small antennas, the quasi-static antenna design algorithm can be used to design very low *Q*-factor ratio antennas with high bandwidth [4, 5]. The *Q*-factor ratio is the coefficient of the largest term in Chu's limit, the right side of Equation (1) [7]. Lowering the *Q*-factor ratio reduces the *Q*-factor for the electrically small part of the frequency range. The UWB antenna shape in the quasi-static antenna design algorithm is a cone with an attached bulb. The lowest operational frequency is reduced without increasing the voltage standing wave ratio (VSWR) at higher frequencies. This is a physics-based algorithmic approach that avoids the typical cut-and-try method.

15. SUBJECT TERMS

ultra wideband antenna (UWB); conical charge distribution; effective height, capacitance; antenna design; Q-factor ratio; Quasi-static antenna design algorithm

16. SECURITY CLASSIFICATION OF:			**17. LIMITATION OF ABSTRACT**	**18. NUMBER OF PAGES**	**19a. NAME OF RESPONSIBLE PERSON**
a. REPORT	**b. ABSTRACT**	**c. THIS PAGE**			Thomas O. Jones
U	U	U	U	39	**19B. TELEPHONE NUMBER** *(Include area code)* (619)553-7082

INITIAL DISTRIBUTION

84300	Library	(1)
85300	Archive/Stock	(1)
52260	T. Jones	(1)

Defense Technical Information Center
Fort Belvoir, VA 22060–6218 (1)

Approved for public release.

SSC Pacific
San Diego, CA 92152-5001